Dedicated to innovation in aerospace

NLR-TP-2021-202 | June 2021

Multiple Unmanned Aerial Systems collision impact on wing leading edge

CUSTOMER: Netherlands Aerospace Centre

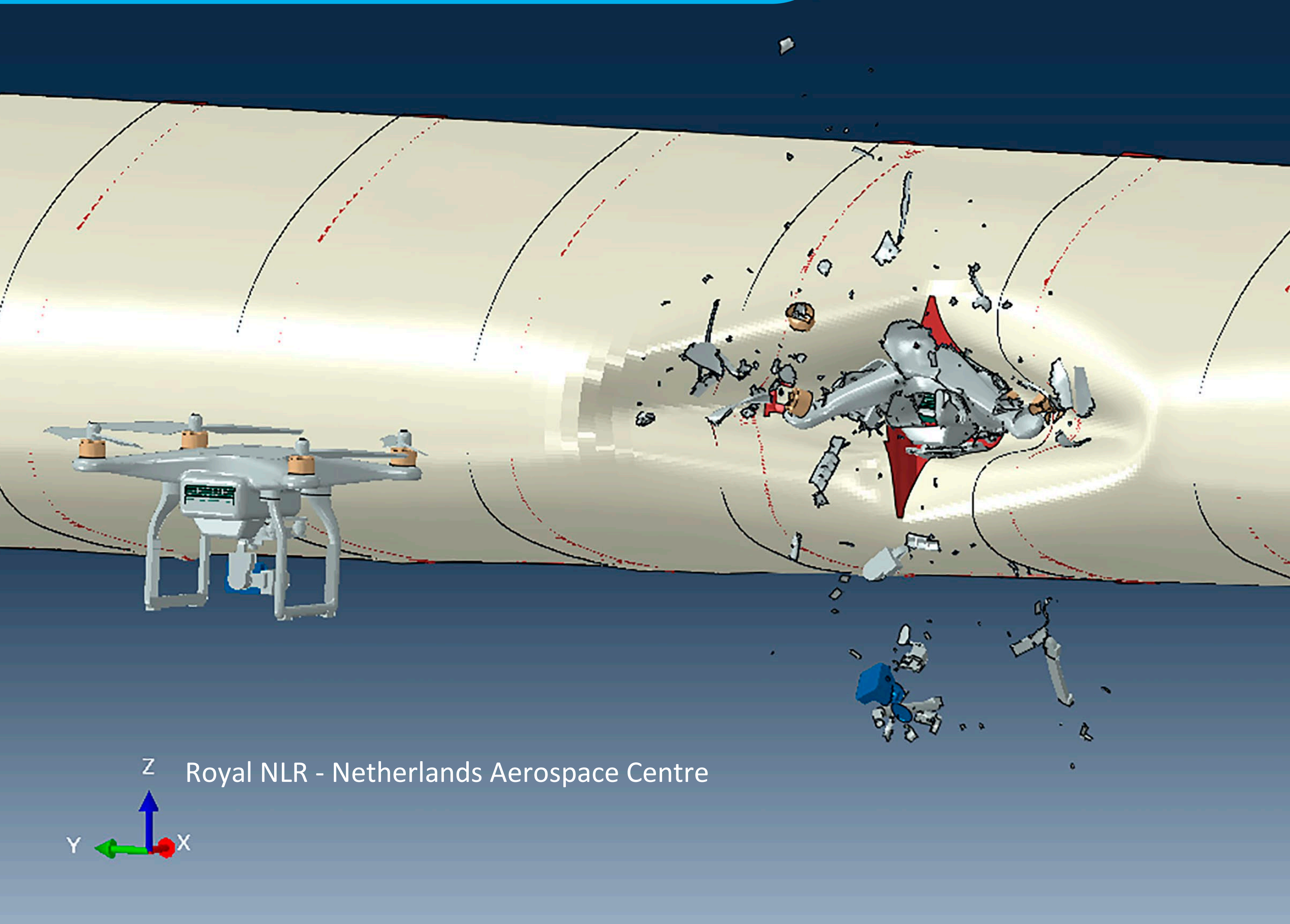

Royal NLR - Netherlands Aerospace Centre

Dedicated to innovation in aerospace

EXECUTIVE SUMMARY

UNCLASSIFIED

Multiple Unmanned Aerial Systems collision impact on wing leading edge

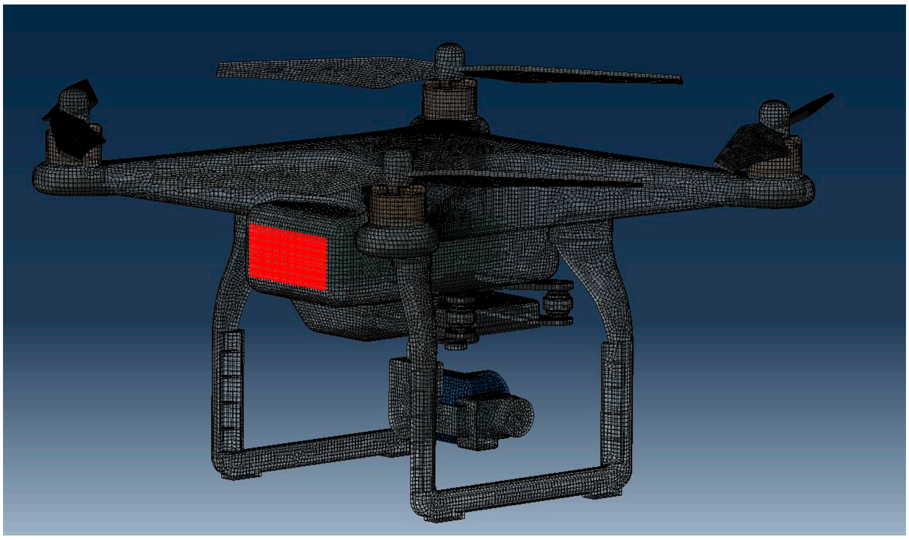

REPORT NUMBER
NLR-TP-2021-202

AUTHOR(S)
A.J. de Wit
W.M. van den Brink
S.M. Moghadasi

REPORT CLASSIFICATION
UNCLASSIFIED

DATE
June 2021

KNOWLEDGE AREA(S)
Computational Mechanics and Simulation Technology
Aerospace Collaborative Engineering and Design

DESCRIPTOR(S)
UAS impact
bird strike
leading edge
finite element simulation

Problem area

Unmanned Aerial Systems (UASs) are increasingly starting to dominate the lower airspace. This increases the chance that a UAS will hit the means of transport of people e.g. aircraft, helicopters. At present, aviation authorities are determining the thread of a UAS impact on aircraft. It is likely that this research will initiate new ruling or requirements on so-called aircraft wetted zones, e.g. the wing leading edge. The wetted zones currently have to be certified for bird impact requirements. Research suggests that these requirements may not be sufficient for UAS impact and such an impact may even damage the aircraft primary structure. In this work we investigate the impact of multiple UASs when they are flying close to each other and impact one after another on the leading edge.

Description of work

In this work a numerical model for simulating UAS impact on a wing leading edge is created. The relevant components of the UAS have been modelled and impact simulations of the individual components have been compared with physical testing results that are recorded in the open literature. Furthermore, a numerical model of a soft body bird impactor and a wing leading edge target model is created. To compare the bird impactor model with literature findings simulation of impact on a flat plate is compared with measurements recorded in the literature. The skin thickness of the leading edge model is sized based on bird impact simulations. Finally, impact simulations onto the leading edge model have been carried out for UASs with different weight for single and multiple UAS impact.

Results and conclusions

Single UAS impact simulations showed that for 1.2 [kg] UAS no penetration of the leading edge occurred for the conditions accounted for in this study. Heavier UASs penetrated the leading edge skin and some deformation of the spar is observed. In case of multiple UASs impacting the leading edge the damage on the leading edge increases and the primary structure is deformed. The multiple UAS impact scenario causes additional damage to the leading edge with respect to the single UAS impact for the cases simulated in this work.
For the impact scenarios considered in this work battery cells remain largely intact which raises concerns over post impact thermal behaviour of battery cells due to short circuiting. Such an analysis was out of scope for the present work but should be futher investigated. Furthermore, the impact behaviour of a composite leading edge is different from the aluminium case considered here and a separte study for such material should be investigated.

Applicability

The UAS impact models developed for this study can be used by authorities and the industry to analyze different threat scenarios involving medium sized UASs. With the developed models further insight in the damage behavior is obtained and expensive impact tests can be reduced. Moreover, studies like these can be input for possible design changes for aircraft

GENERAL NOTE
This report is based on an paper to be published in Aeronautical Journal Structures and Materials, August 2021, by Royal Aeronautical Society.

Royal NLR
Anthony Fokkerweg 2
1059 CM Amsterdam, The Netherlands
p) +31 88 511 3113
e) info@nlr.nl i) www.nlr.nl

Dedicated to innovation in aerospace

NLR-TP-2021-202 | June 2021

Multiple Unmanned Aerial Systems collision impact on wing leading edge

CUSTOMER: Netherlands Aerospace Centre

AUTHOR(S):

A.J. de Wit	NLR
W.M. van den Brink	NLR
S.M. Moghadasi	NLR

Royal NLR - Netherlands Aerospace Centre

This report is based on an paper to be published in Aeronautical Journal Structures and Materials, August 2021, by Royal Aeronautical Society.

CUSTOMER	Netherlands Aerospace Centre
CONTRACT NUMBER	
OWNER	NLR
DIVISION NLR	Aerospace Vehicles
DISTRIBUTION	Unlimited
CLASSIFICATION OF TITLE	UNCLASSIFIED

APPROVED BY:		Date
AUTHOR	A.J. de Wit	08-06-2021
REVIEWER	N. van Hoorn	08-06-2021
MANAGING DEPARTMENT	A.A. ten Dam	08-06-2021

Summary

Unmanned Aerial Systems (UASs) are increasingly starting to dominate the lower airspace. This increases the chance that a UAS will hit the means of transport of people e.g. aircraft, helicopters. For air traffic, the European Union Aviation Safety Agency (EASA) and the Federal Aviation Administration (FAA) are in the process of determining the threat of a UAS impact on aircraft. This will result in new rules that may impose new or additional requirements on the "wetted zones" of aircraft and the like. Current research suggests that aircraft wetted-areas e.g. wing leading edge that are certified for “bird-impact” may not sustain an “UAS-impact”. Such an UAS-impact may even damage the primary load carrying structure. But what would happen if multiple UASs are flying close to each other? To the authors’ knowledge, the effect of multiple UAS impacts on a wetted zone has not been established yet.
A finite element modelling approach is chosen for the UAS, specifically, a Lagrangian approach using material non-linearity and damage. A comparison is made between the damage caused by a bird impactor and a UAS impactor model. To establish the resulting damage of multiple UASs impact on a wing leading edge a multiple UAS impact scenario is executed. The results show that a wing leading edge capable of sustaining a bird impact may not sustain a UAS impact, which supports previous findings. Furthermore, for all simulated cases the front spar did not get penetrated due to the components that did manage to enter the leading edge. However, for the heavier drone some deformation of the front spar was observed. The multiple UAS impact scenario causes additional damage to the leading edge with respect to the single UAS impact and larger deformation of the front spar is observed without material failure taking place.

Contents

Abbreviations

ACRONYM	DESCRIPTION
AMC	Acceptable Means of Compliance
CS	Certification Specifications
EASA	European Union Aviation Safety Agency
EOS	Equation of state
FAA	Federal Aviation Administration
FAR	Federal Aviation Regulation
FEA	Finite Element Analysis
UAS	Unmanned Aerial System

SYMBOLS	DESCRIPTION
A,B,C,n,m	Johnson-Cook strength model parameters
d1,…,d5	Johnson-Cook failure model parameters
c0, S, γ_0	Mie-Grüneisen equation of state parameters
E	Young's modulus
Et	Tangent modulus
h	Height
l	Length
m	Mass
r	Radius
V	Volume
ε_{max}	Strain at fracture
ε_0	Reference strain rate
ν	Poisson's ratio
ρ	Density
σy	Yield stress

1 Introduction

In the past, collisions with birds have led authorities to impose regulation on so-called “wetted” areas. These are the areas of an aircraft in the direction of flight. Regulations on “wetted” areas are listed in the European Union Aviation Safety Agency (EASA) Certification Specifications (CS) and Acceptable Means of Compliance (AMC) for Large Aeroplanes (CS-25) (1). The requirements for bird strike are listed in CS 25.631 Bird strike damage and AMC 25.631 for impact with a 4 lb bird. The Federal Aviation Administration has comparable regulation in place documented in Federal Aviation Regulation (FAR) (2). For bird impact the relevant requirements are documented in FAR 25.571 for wing leading edge and engine, in FAR 25.631 for leading edge empennage and in FAR 25.775 for windshield and windows. A decade ago, an EASA study (3) concluded that the bird strike requirements as documented in CS-25 are providing an adequate level of safety.
Nowadays, Unmanned Aerial Systems (UASs) are increasingly starting to dominate the lower airspace. This increases the chance that UAS will hit the means of transport of people e.g. aircraft, helicopters. For air traffic, the UAS threat becomes apparent as authorities such as EASA report threat occurrences in annual safety reports (e.g. (4)). In recent year (2019), the number of incidents recorded with UASs is higher than incidents recorded with bird/wildlife strike. Such findings are supported in earlier studies as well, see e.g. (5), showing an increasing trend in UAS related events.
Current research (6) suggests that aircraft wetted-areas (e.g., wing leading edge) that are certified for “bird-impact” may not sustain a “UAS-impact”. Further insight was obtained with ground tests carried out by the British department for Transport, the Military Aviation Authority and the British Airline Pilots’ Association (7) on a helicopter windshield to replicate UAS impact using a gas gun. In addition, a simulation model for UASs was set-up to carry out impact simulations on helicopter windshield and tail rotor. EASA formed a “drone collision” task force (8) and the FAA an Alliance for System Safety of UAS through Research Excellence (9) to assess the impact of UAS with aircraft collision through development of UAS analysis models and laboratory testing.
EASA and FAA are in the process of determining the threat of a UAS impact on aircraft via extensive research programs. The FAA has concluded an extensive program called UAS Airborne Collision Severity Evaluation (9). In this program, relevant components of UASs were identified, damage level categories defined, and collision scenarios specified (10). Among several other studies, numerical models of a quadcopter UAS (11) and fixed wing UAS (12) were developed and an extensive impact testing campaign was launched to calibrate the numerical simulation models. Different collision scenarios were studied and the severity of impacts were classified. These studies concluded that UAS collisions may introduce severe damage to aircraft structures. In recent work (13), design changes necessary for a wing leading edge to sustain a UAS impact are studied showing the weight penalty on aircraft structure when accounting for the possibility of a UAS collision. The thread on helicopter windscreens due to a collision with a quadcopter is simulated in (14) together with a detailed outline of a quadcopter numerical simulation model. Currently (2020), EASA is running a program called Vulnerability of Manned Aircraft to Drone Strikes (15) to determine the threat of UAS collision.
In an incident at Gatwick Airport (16) multiple UASs were flying deliberately close to each other which forced authorities to ground flights. The costs of the Gatwick closure were estimated to be significant (17) and in a more recent study (18) an analysis is carried out if the cost of a defense system outweighs the costs of shutting down an airport. A defense system may not be 100 percent effective or closing an airport not desirable. In light of this incident, what would happen to an aircraft wetted zones in case of multiple UAS impact? To the authors’ knowledge, the damage multiple UAS impacts have on a wing leading edge has not been established yet.
To investigate the impact of a multiple UAS strike on the wing leading edge and front spar a UAS impact model is created in Section 2. Relevant components for the impact are modelled and the impact is compared with literature findings. This UAS model is then impacted onto a wing leading edge that is sized to withstand a bird-impact in Section 3. The results of multiple UAS impact are given in Section 4. Finally, conclusions and recommendations for further research are given in Section 5.

2 Methodology

Commercial UASs come in various configurations and sizes, see e.g. Figure 1. Several divisions exist in the literature to categorize UASs. In the present work the authors follow a division that was used by EASAs ‘Drone Collision’ Task Force for readily available consumer UASs (8) under 5 [kg]. According to EASA this qualifies for the majority of commercially available UASs (19). The two main categories considered in this work with their subdivision into weight categories are:

1. Quadcopter UAS
   a. Tiny (0.25 [kg], harmless)
   b. Small (0.5 [kg])
   c. Medium (1.5 [kg])
   d. Large (3.5 [kg])
2. Fixed wing UAS
   a. 3.5 [kg]

Figure 1: An overview of some of NLR's in-house UASs. Image - Royal NLR

As an example of a quadcopter UAS and a fixed wing UAS, Figure 2 shows in the left image a UAS quadcopter that requires rotors to stay in the air and on the right image a fixed wing UAS that more resembles a conventional aircraft.

Figure 2: Left example of a quadcopter UAS and right an example of fixed wing UAS. Image- Royal NLR

Tiny UASs (below 0.5 [kg]) are expected to cause no damage to the aircraft wetted zones (8) and the large UAS's are expected to cause significant damage. This expectation is supported by results reported in literature for quadcopter UAS (e.g. (11)) and fixed wing UAS (e.g. (20)).
Of particular interest is the medium sized UAS because the impact energy is close to that of a bird impact for which design regulation is in place. Bird-impact studies are typically carried out with a 4 pound (1.81 [kg]) bird or equivalent gel impactor in accordance with CS 25.631 (1). Research (e.g. (10)) suggest that the hard components of a UAS such as the battery and motors will cause damage to certified areas at lower impact energy.

Because a UAS consists of individual parts with different strength and stiffness properties the complete UAS modelling is split into three categories of components to reduce the number of components in the model (see e.g. (19)).

1. Frangible and low density housing;
2. Infrangible and medium density media such as the battery package;
3. Sharp high density objects such as the motor.

In addition to these three components, payload items need to be taken into account when modelling the UAS. Typically, consumer UASs are fitted with a camera, therefore, in the present case the payload consists of a photo/video camera for recording.

2.1 UAS dimensions

To model the UAS geometry and make the results comparable to previous research (e.g. (11), (13), (14) or (21)) a common consumer UAS model is used. This model is the DJI Phantom 3 standard that has been used in previous UAS threat studies as well. Furthermore, the authors had access to a similar physical model making it relatively easy to determine size and weight of components. Therefore, in the present work a UAS configuration is constructed for the modelling which is assumed analogous to previous studies recorded in the open literature.

The UAS size is usually indicated as the diagonal distance between rotors. In this case the diagonal distance is 354 [mm]. For the present study, the meshed geometry of the UAS is shown in Figure 3.

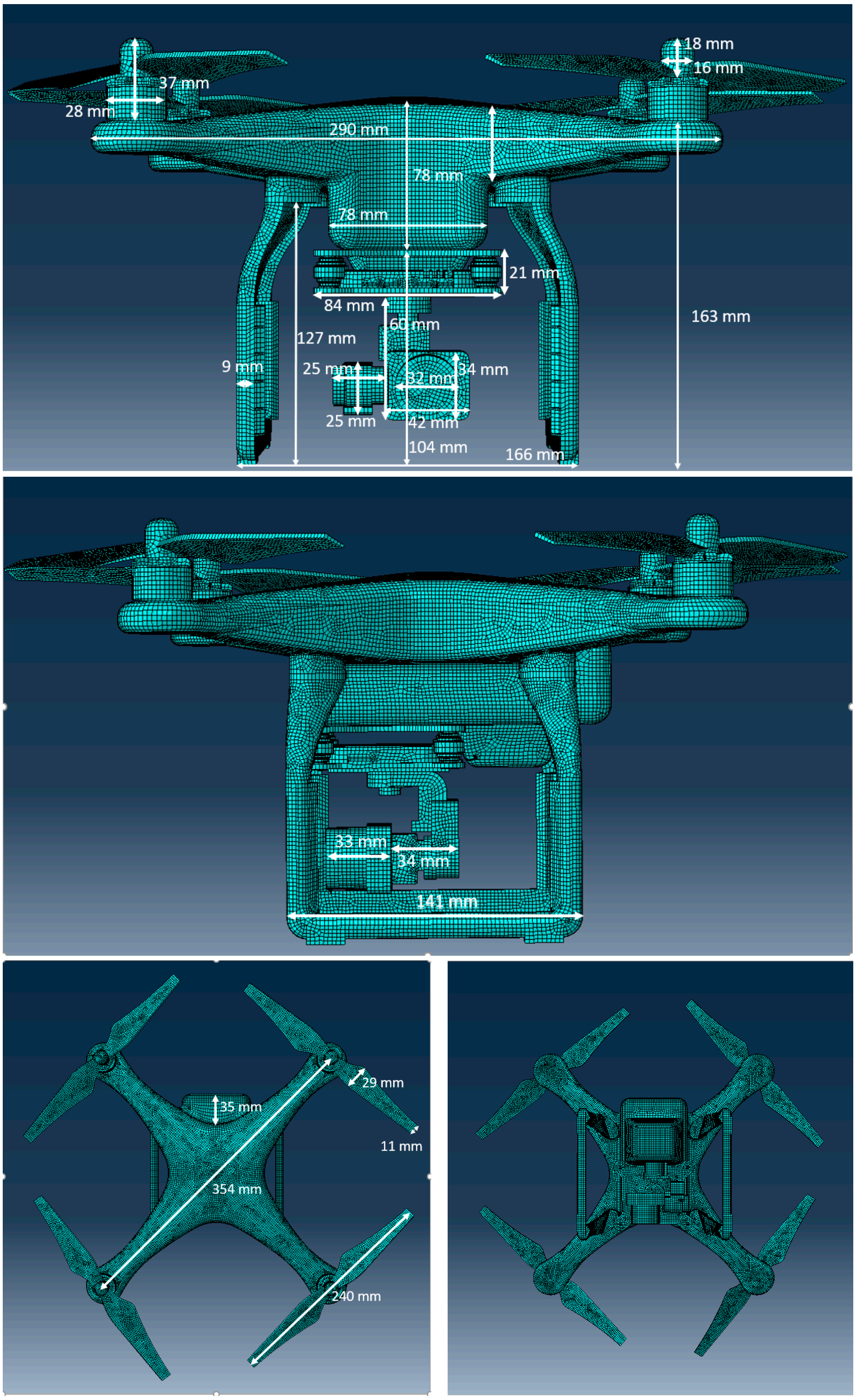

Figure 3: Different view angles of the UAS model used for the impact studies. Some overall dimensions are shown to give an impression of size and location of components with respect to each other

In Figure 3 some relevant dimensions are given from the components that make up the UAS Finite Element Analysis (FEA) model. The mesh density is set to 2 [mm] which produces accurate results according to a mesh density study by Jonkheijm (14). A total of 77487 nodes comprise the UAS battery, camera, motors, housing, and propellers. The total number of elements is 76516 of which 1400 are solid elements and the remainder are shell elements.

2.2 UAS housing and propellers

To simplify the modelling of the UAS housing not all components are modelled separately. Instead, the UAS housing is constructed as a single body. Furthermore, this body is then meshed via mid-surface modelling using S4R shell elements in Abaqus (22). Each shell element is assigned a thickness and an offset. To simplify the modelling, the thickness is set as an uniform parameter and the offset used is the external geometry of the UAS. In addition, the propellers are modelled via mid-surface modelling with S4R elements and are given the same thickness and material properties as the UAS housing. The housing and propellers are shown in Figure 4.

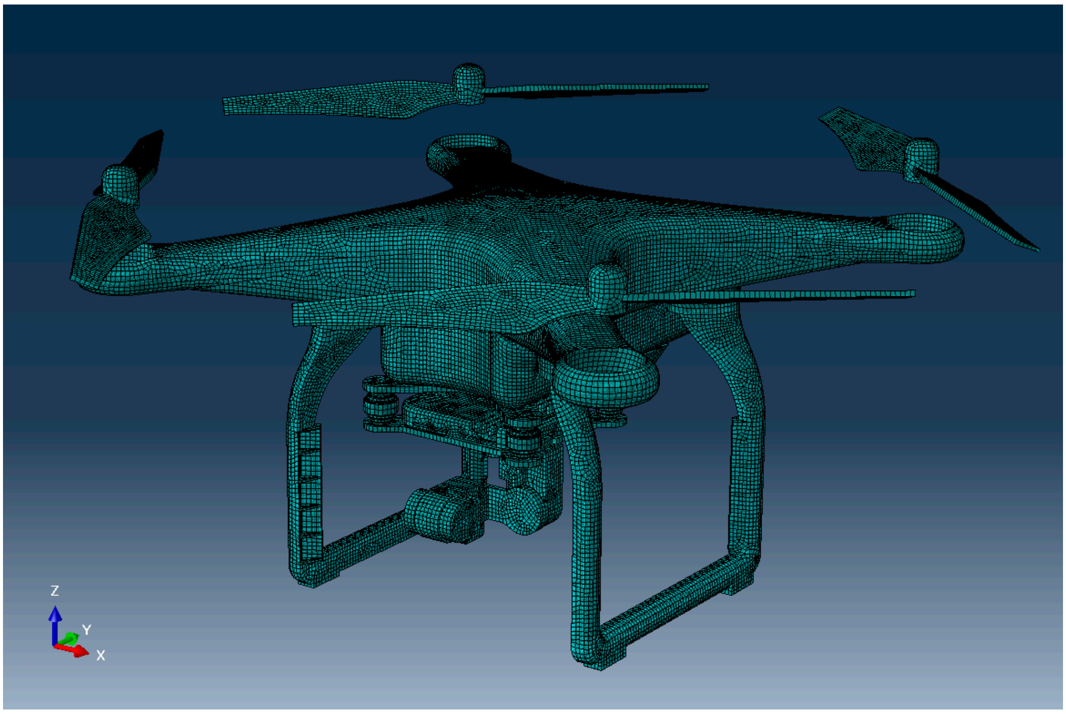

Figure 4: Mid-surface shell element model of the UAS housing including the propellers

In the FEA model, the skin thickness of the UAS housing is adjusted such that the weight of the UAS housing and propellers combined corresponds to 617.6 [g]. For the present simulation model this corresponds to a skin thickness of 2.29 [mm] for housing and propellers. Hence, this is different from the thickness of components of the physical model. However, as these parts are considered frangible the impact damage is not expected to significantly change. The weight of 617.6 [g] is determined by taking the total UAS weight from literature (1216 [g]) and subtracting the battery, motors and camera weight. The weight of battery, motors and camera are subject of the next paragraphs. The UAS housing material is taken analogous to previous work (e.g. (14) or (13)) and consists of polycarbonate material. An elastic-plastic material model and ideal plasticity was assumed to model the mechanical behaviour of the housing. Progressive damage was modelled using maximum tensile strain as the parameter when material degradation started. Furthermore, elements are removed once a maximum degradation of 0.95 is reached. The material properties taken from Drumond (13) and Jonkheijm (14) are listed in Table 1 for completeness.

Table 1: Mechanical Properties of Polycarbonate (13) (14)

$\rho\ [kg/m^3]$	E [GPa]	ν [-]	$\sigma y\ [MPa]$	$\varepsilon_{max}\ [-]$
1180	2.35	0.3	62	0.2

2.3 Battery Package

The battery package is modelled as a solid consisting of seven individual battery cells (15.2 [V] pack). The cells are meshed via solid elements C3D8R in Abaqus. Each cell is 3 [mm] thick, 58 [mm] in width and 120 [mm] in length. The distance between each battery cell is 0.5 [mm]. Contact between the cell layers is modelled via a penalty formulation with a 0.2 friction coefficient in tangential direction and 'hard contact' in normal direction.

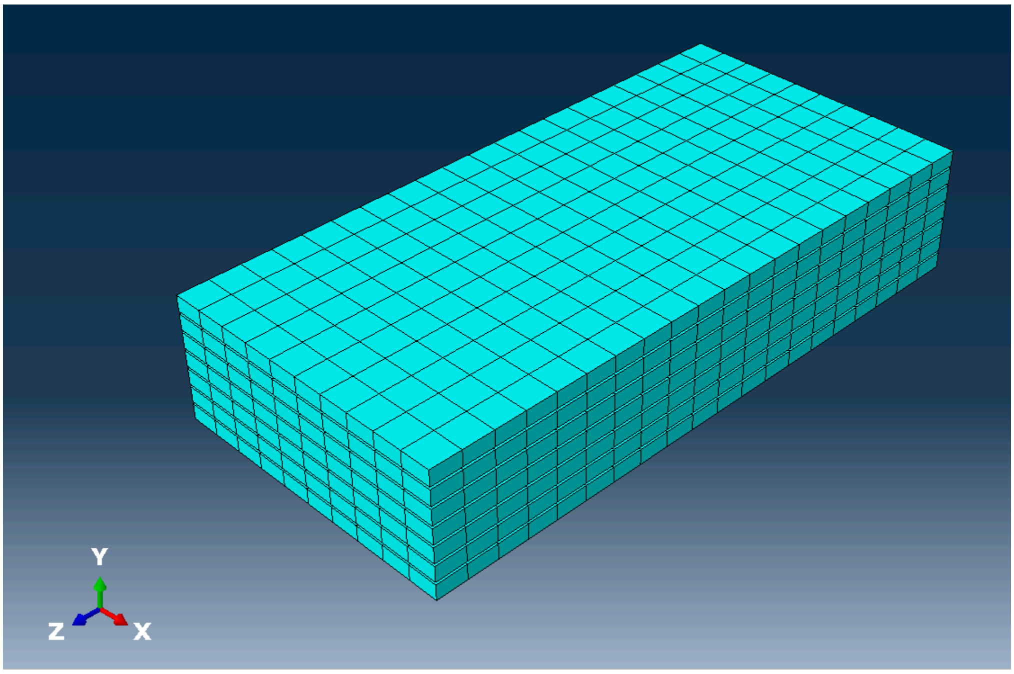

Figure 5: Battery package of the UAS consisting of seven battery cells modelled as solids

The battery package is attached to the UAS housing via a tie constraints on the back of the UAS, see Figure 6.

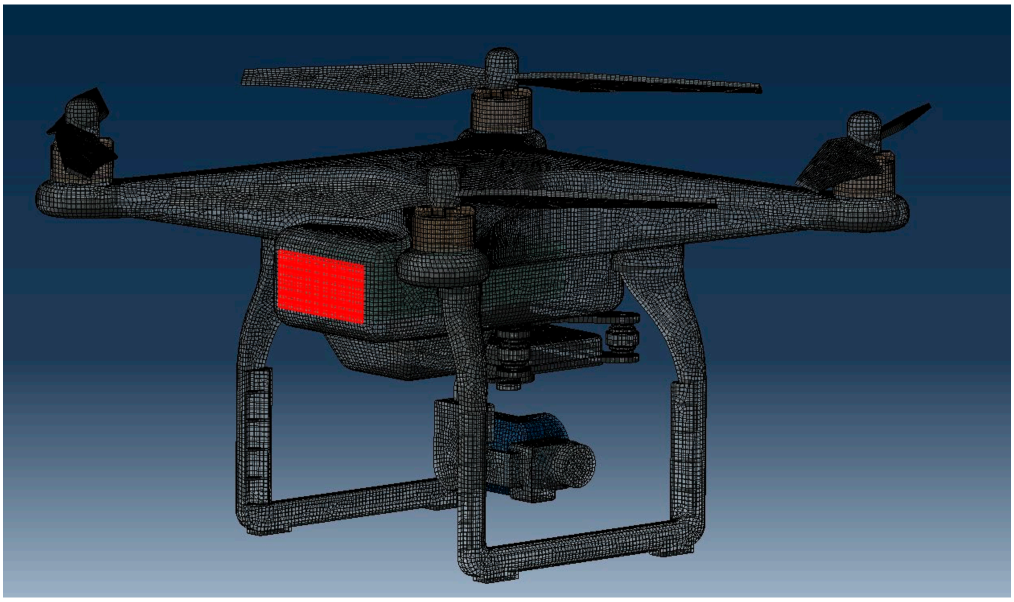

Figure 6: The battery is attached to the UAS housing via a tie constraints. The surface where the nodes are tied between the housing and the battery is indicated in red

In previous studies ((13) (14)) the pouch lithium-ion batteries were modelled as a crushable foam. In the present study, the batteries are considered to behave as an elastic-plastic material with ductile damage model. Element elimination is set at maximum degradation of 1.0. The battery dimensions are based on in-house measurements of a UAS battery pack. Therefore, density of the battery material is adjusted to compare with literature findings (343 [g] battery) and in house measurements (438 [g] battery). The material properties are listed in Table 2.

Table 2: Material properties for the UAS battery pack. Second row for the light battery pack (343 [g]) and third row corresponds to the heavier (438 [g]) battery pack

$\rho\ [kg/m^3]$	E [GPa]	ν [-]	$\sigma y\ [MPa]$	Et [MPa]	ε_{max} [-]
2347	3000	0.3	50	200	0.05
3000	3000	0.3	50	200	0.05

2.4 Motor

The UAS motor was modelled via a mid-surface modelling technique. To simplify the modelling the motor geometry was reduced to the external surface of the motor caps. These caps were given the equivalent density of the rotor (green) and core stator (white), see Figure 7.

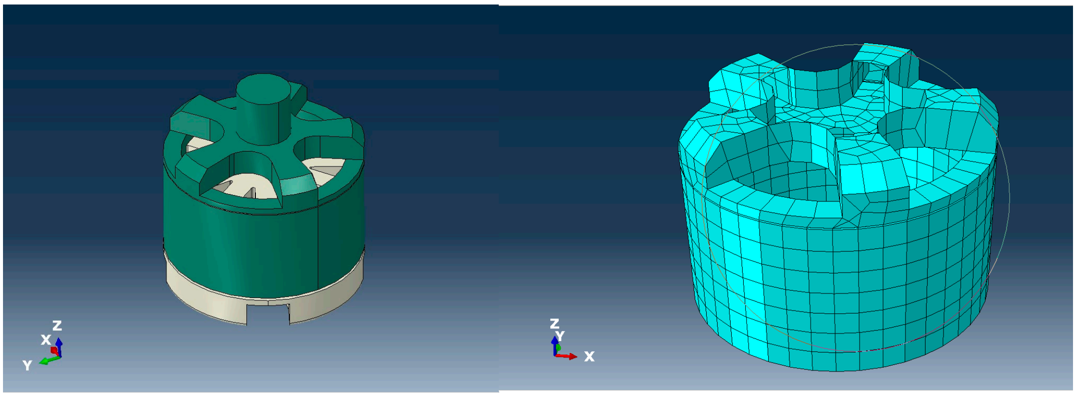

Figure 7: The motor consists of a stator and a rotor part. To simplify the modelling a mid-surface technique was used with shell elements on the caps external geometry

The weight of each motor is taken from the literature and corresponds to 50.7 [g] for each motor. The skin thickness of the shell elements is chosen to be 2.755 [mm] which combined with the density listed in Table 3 corresponds to the previously mentioned weight.

Table 3: Material properties of the motor consisting of Steel Alloy AISI4130 (23)

ρ [kg/m^3]	E [GPa]	ν [-]	$\sigma y\ [MPa]$	Et [MPa]	ε_{max} [-]
7850	200	0.32	483	1174	0.12

The material of the motor was considered steel and relevant material properties are listed in Table 3. The material was modelled as a bi-linear elastic plastic material. Element deletion was used with criteria for element deletion to correspond to maximum tensile strain value.

The motors move along with the UAS housing in the same direction as the UAS and are connected via a contact definition. In tangential direction this is done via a penalty formulation with a friction coefficient of 0.2 and in normal direction via 'hard contact'. The propellers are connected directly to the motors via node connectivity, see Figure 8.

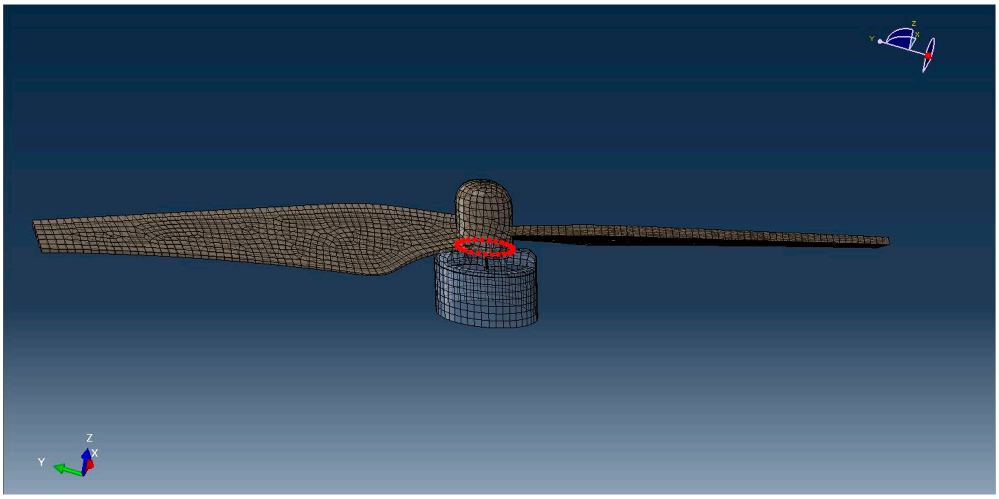

Figure 8: The motors (grey) are connected to the propellers (brown) via shared nodes highlighted in red

2.5 Payload

The UAS payload in this study consists of a standard camera. The outer dimensions of the camera are 32.6 [mm] x 42 [mm] x 34 [mm]. Material properties are taken from literature (23). The camera is modelled via a mid-surface model using shell elements on the outer contour of the camera geometry. The thickness assigned to the shell element mesh is adjusted such that the mass of the camera corresponds to the mass used in literature which is 52.6 [g]. The corresponding thickness assigned to the shell elements is 2.935 [mm].

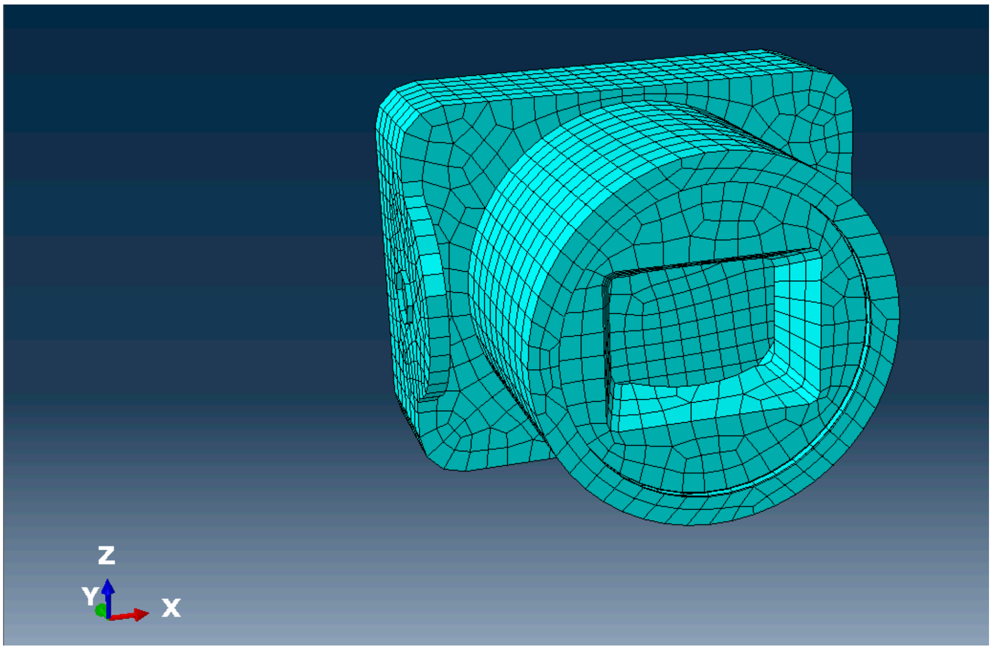

Figure 9: Geometry and shell mesh used for the payload. Here the payload consists of a camera

The camera is attached to the UAS housing via shared nodes. These nodes are highlighted in red in Figure 10.

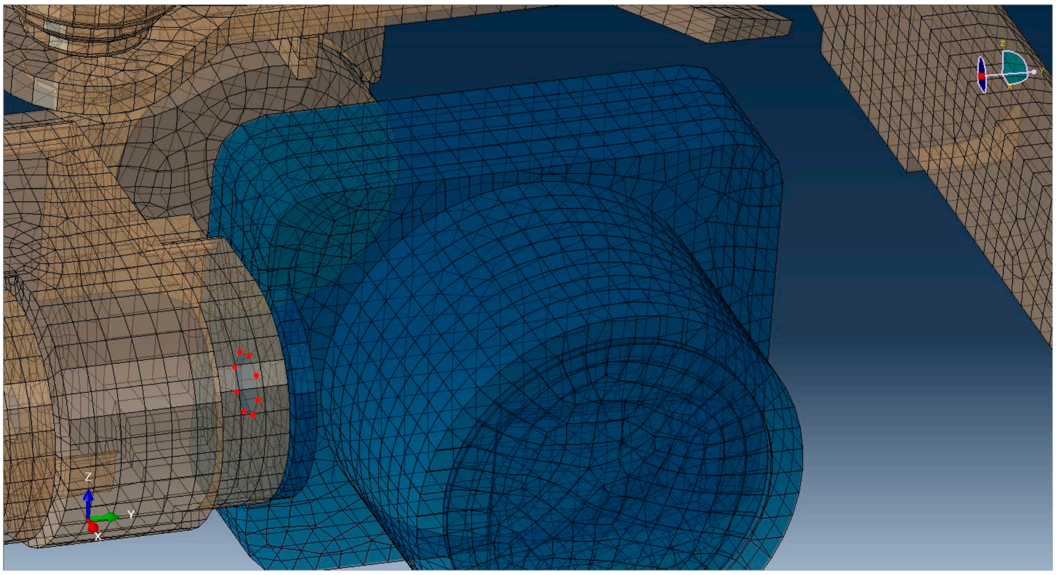

Figure 10: Attachment of the camera to the UAS housing is done via shared nodes that are highlighted in red

Material properties for the camera are taken from previous research and are listed for completeness in Table 4.

Table 4: Material properties for the pay-load consisting of a camera. The camera housing consists of Aluminium Casting alloy A520.0-F (23)

ρ [kg/m^3]	E [GPa]	ν [-]	σy [MPa]	Et [MPa]	ε_{max} [-]
2600	200	0.3	170	1164	0.14

The camera housing is modelled via a bi-linear elastic-plastic material model with element deletion criteria. The criteria for element deletion is maximum tensile strain value.

3 Reference impact examples

In this section the modelling strategy of Section 2 is compared with results from literature. First, numerical simulations of the battery, motor, and camera impact tests on an aluminium plate with variable thickness were performed. Second, a leading edge that is sized for bird impact is modelled to simulate the impact of a UAS onto a leading edge.

3.1 Target – aluminium plate

The numerical model of the UAS components is compared with impact results recorded in literature to compare overall impact behaviour of each components numerical model with that of a controlled impact experiment. The ballistic impact studies to which the simulation results were compared are recorded in (11). Simulation results of these impact tests by other authors are documented in e.g. (13) and (14). Here, first the target model is discussed followed by results of the numerical impact tests.

3.1.1 Numerical plate model

In the present study a 890 [mm] x 890 [mm] aluminium plate is modelled with a thickness of 1.6 [mm] or 6.35 [mm]. The aluminium plate is the impact target as documented in (11). The material properties for the aluminium plate were taken from (24) and are listed in Table 5.

Table 5: Material properties Aluminium 2024-T3

ρ [kg/m^3]	E [GPa]	ν [-]
2780	73.1	0.3

The Aluminium alloy 2024-T3 was modelled as an elastic-plastic material with Johnson-Cook plasticity model. The necessary material parameters are taken from (24) and are listed in Table 6.

Table 6: Material parameters for the Johnson-Cook plasticity model

A [MPa]	B [MPa]	n	m	C	ε_0 [1/s]
369	684	0.73	1.7	0.0083	1

Failure of the aluminium plate was modelled via Johnson-Cook dynamic failure model which is available in Abaqus (22). The necessary material parameters are listed in Table 7.

Table 7: Input parameters for the Johnson-Cook dynamic failure model

d1	d2	d3	d4	d5	ε_0 [1/s]
0.112	0.123	1.5	0.007	0	1

Element deletion is used and elements are deleted upon reaching maximum degradation. The plate is meshed with shell elements (S4R elements, 2x2 [mm] mesh density) in Abaqus which is shown to be sufficiently accurate in the next section. Furthermore, contact between the target (plate) and projectile (e.g., motor) is modelled using Abaqus built-in interaction procedure. The interaction properties are hard contact (separation after contact) in normal direction and in tangential direction a penalty formulation with a 0.2 friction coefficient and no-slip condition.

3.1.2 Results of impact simulations

The impact simulation studies were carried out on plates of variable thickness of 1.6 [mm] and 6.35 [mm] thickness. The projectile velocity, the projectile weight, and the deflection of the plate are taken from literature references and compared with the results of the simulations. The results shown in Table 8 agree with the results obtained in the literature. History of maximum deflection of the plates during impact is shown in Figure 11.

Table 8: Results of the UAS component impact studies compared to literature findings (11)

UAS component	Plate thickness [mm]	Impact velocity [m/s]	Projectile weight [g]	Penetration	Simulated Maximum deflection [mm]	Maximum deflection according to literature [mm]
battery	1.6	127.71	343	N	48.6	47.8
battery	6.35	128.61	338	N	19.8	19.6
camera	1.6	129.24	52.6	N	18.2	18.5
motor	1.6	128.32	50.7	Y	N/A	N/A
motor	6.35	136.25	50.98	N	6.5	7.9

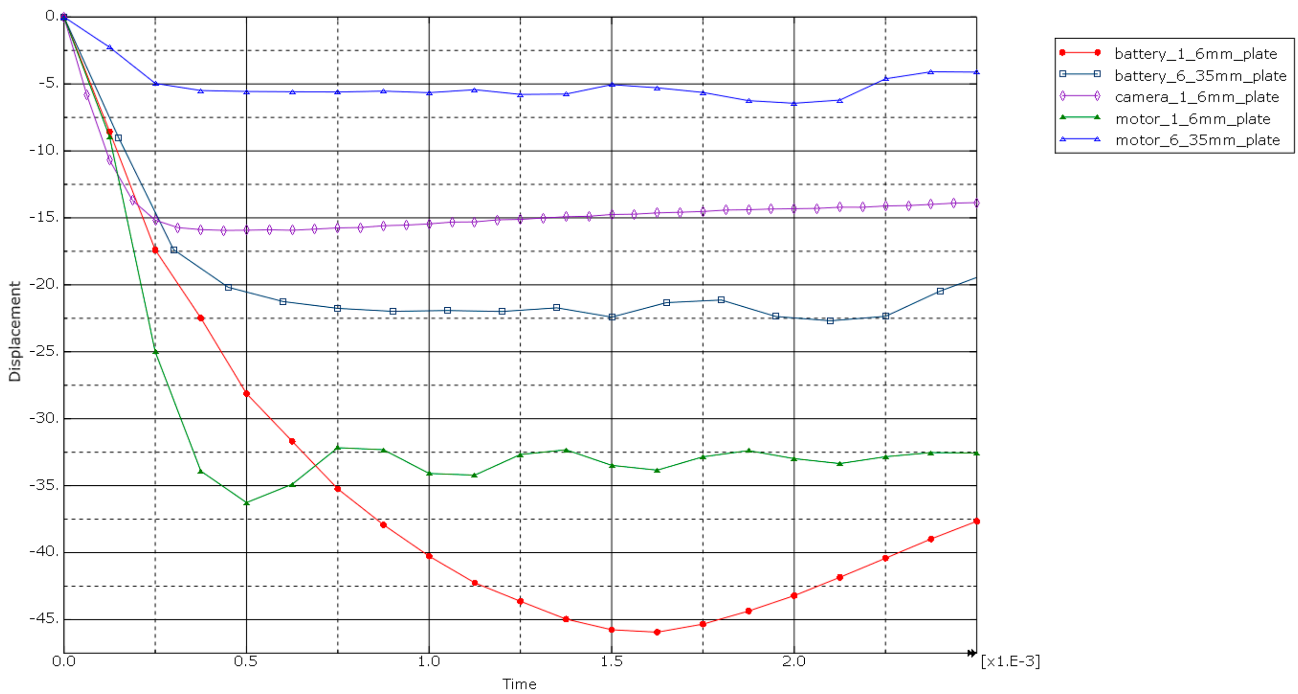

Figure 11: Maximum displacement of the plate during impact with different components of the UAS

Please note that the distance between the UAS component and the plate was not equal for each simulation. Hence, the exact moment of impact of each component differs slightly on the horizontal axis in Figure 11. For the maximum deflection results recorded in Table 8 this has no effect. In addition, at maximum deflection of the 1.6 [mm] plate impacted by the motor, the motor penetrates the skin and the deflection recorded resembles that of the torn skin.

The skin penetration is shown in Figure 12 where the motor impact is plotted at different time steps. The high motor density is likely the cause of the penetration of the skin. The numerical results agree with the experimental results recorded in literature.

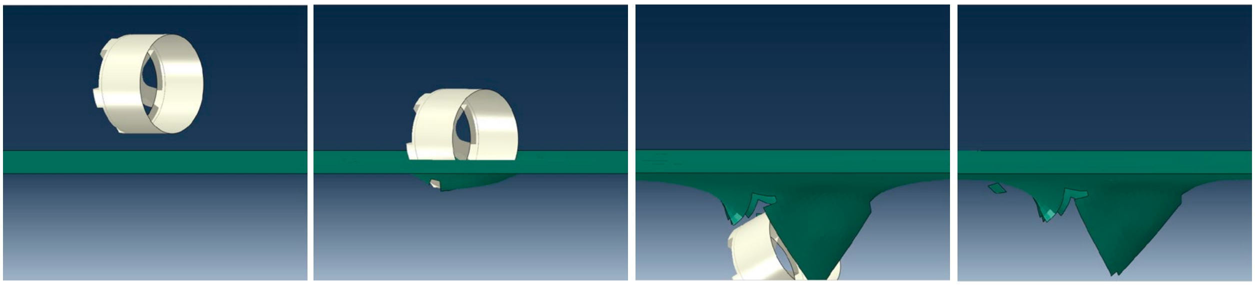

Figure 12: Motor component penetrating the 1.6 mm aluminium plate

3.2 Target – Leading edge

To study the effect of a ballistic impact of a UAS onto a leading edge, first a leading edge design is necessary that is at least able to withstand a bird impact. In the work of McNaugtan (25) an empirical equation is given for the preliminary design of aluminium leading edges. In this work however, an approach analogous to (13) is followed to determine the necessary skin thickness via FEA.

3.2.1 Leading edge numerical model

In this work, the skin thickness of the leading edge is determined via FEA of the bird impact for which no penetration or skin tearing is observed. The rib flanges are connected with kinematic constraints to the leading edge skin and spar. The thickness of ribs and spar is taken as 2 mm thick and not tuned further. Analogous to the work of (13) Aluminium 7050_T7451 is taken for the ribs and spar. The material properties are listed in Table 9. For the skin the material Aluminium T2024-T3 is chosen and the skin thickness will be adjusted to sustain the bird impact as discussed in the next section.

Table 9: Material properties Aluminium 7050_T7451 (23)

ρ [kg/m^3]	E [GPa]	ν [-]	ε_{max} [-]	σy [MPa]	Et [MPa]
2770	71	0.33	0.10	462	663

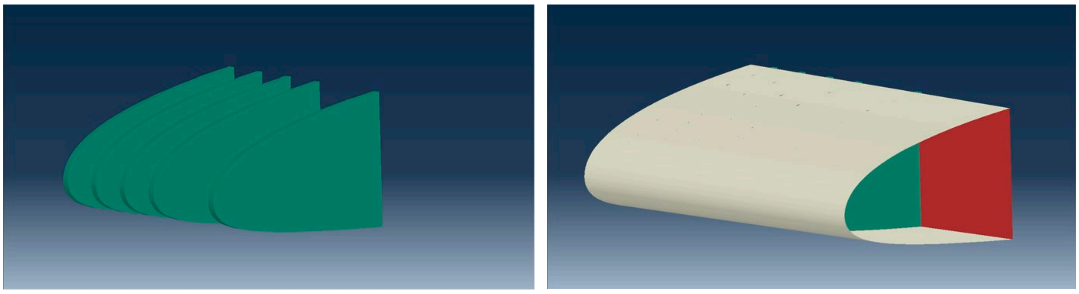

Figure 13: Left: Ribs included in the leading edge design. Right: Skin, rib and spar (red) combined into a leading edge model

3.2.2 Projectile – Bird impactor

A bird impactor model can be created analogous to the work of e.g. Riccio (26). Such a bird impactor model can be used to support the certification process against bird impact. In the present work a cylindrical shaped projector with rounded ends is used. The volume V corresponds to Equation 1.

Equation 1

$$V = \pi r^2 h + \frac{3}{4}\pi r^3, \qquad where\ l = h + 2r, \ \ \frac{l}{2r} = 2.0$$

The mass m of the bird is calculated as $m = \rho V$. Hence, with r = radius 57 [mm], l = length 228 [mm] and h = 114 [mm], the density equals 934 [kg/m3] to arrive at a weight of m = 1.81kg (4 pounds). Furthermore, for this bird impactor model Abaqus built in equation of state Mie-Grüneisen (Us-Up) was used that relates pressure, temperature and volume to compute the mechanical volumetric strength of the material. A discussion on choosing parameters for these equations is given in (27) . Settings chosen based on in-house experience are c0 = 1482.9 [m/s], s = 2 [-], Gamma0 = 0 for a bird impactor with the current dimensions. The bird impactor was meshed with 4340 solid elements which were then converted to particles by using Abaqus built in Smoothed Particle Hydrodynamics (SPH) modelling. The bird impactor is compared with simulations results listed in (28) for a flat aluminium 7075-T6 plate of dimensions 609.5 [mm] in width and 914.4 [mm] in height. For the bird impactor of 1.81 [kg] and a velocity of 136 [m/s] (265 [knots]) the computed plate deformation is listed in Table 10 together with the results recorded in literature (28). The plate simulation results with thickness 2.54 [mm] for which material failure was observed is shown in Figure 14.

Table 10: Comparison between literature values (28) and our simulation results

Plate thickness	Deformation from literature test results	Deformation from literature SPH model results	Present SPH model results
6.35 [mm]	25.4 [mm]	30.4 [mm]	31.9 [mm]
4.08 [mm]	38.1 [mm]	45.72 [mm]	39.5 [mm]
2.54 [mm]	Material failure	Material failure	Material failure

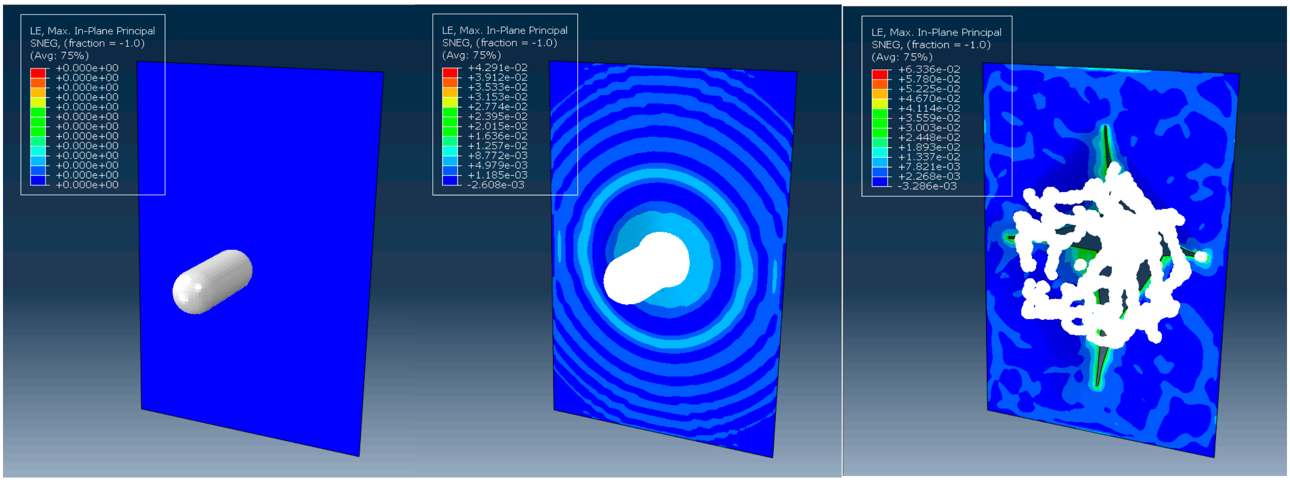

Figure 14: Bird impact on a flat aluminium 7075-T6 plate of 2.54 [mm] thick. Strain contour plotted at 3 different time steps. The plate has a thickness of 2.54 [mm] and 609.5 [mm] width and 914.4 [mm] height

3.2.3 Leading edge sizing for bird impact

To determine the skin thickness of the leading edge the bird impactor is placed in between two ribs with respect to the leading edge, see Figure 15. The speed of the bird impactor is taken chosen as 127 [m/s] (250 knots). This speed is motivated by the choice of impact speed for the UAS which is the difference between UAS speed and aircraft speed. The type of UAS considered here reaches a maximum speed of 20 [m/s] and the aircraft speed (107 [m/s]) is taken as the maximum speed for a holding phase on a flight below 1829 [m] (6000 feet). A value for the aircraft that comes from paragraph 5-3-8-j.2 (a) of Aeronautical Information Manual (29).

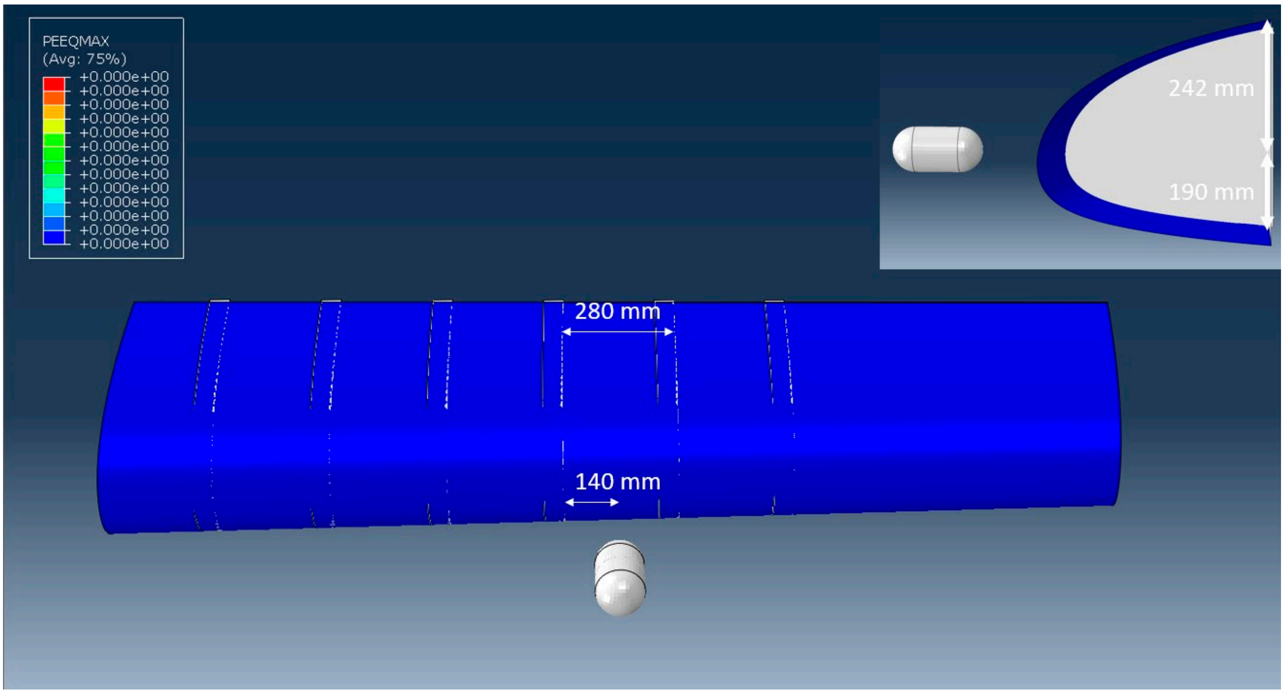

Figure 15: Position of the bird impactor (grey) is chosen in between two ribs

The impactor is converted to SPH particle model on impact. As an initial value for the skin thickness a value of 1.5 [mm] is chosen. The maximum PEEQ strain is shown in Figure 16. As can be seen in Figure 16, skin tearing takes place after impact and therefore the skin thickness has to be adjusted for. The maximum PEEQ strain for the second attempt simulation with a skin of 2 [mm] thick are shown in Figure 17.

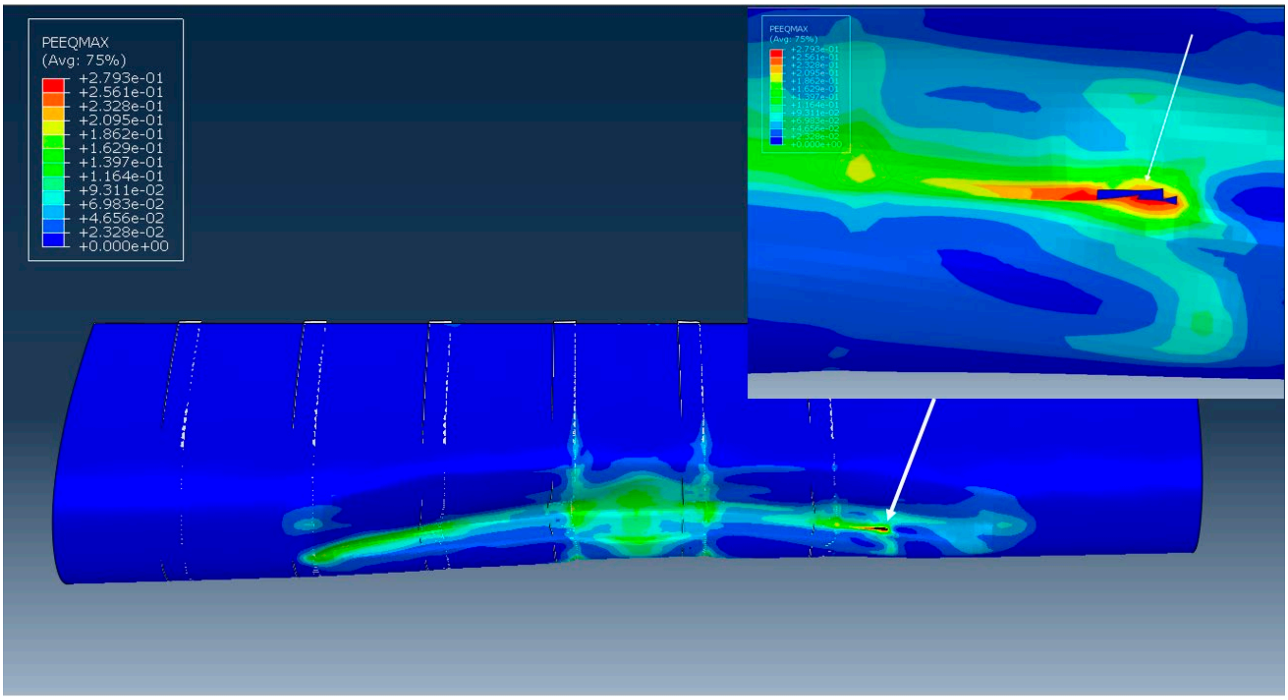

Figure 16: Skin rupture for a skin thickness of 1.5 [mm] after impact of the bird impactor at the location marked with the arrow. PEEQmax (plastic) strain [-] in the skin are above the material failure limit and skin tearing has taken place

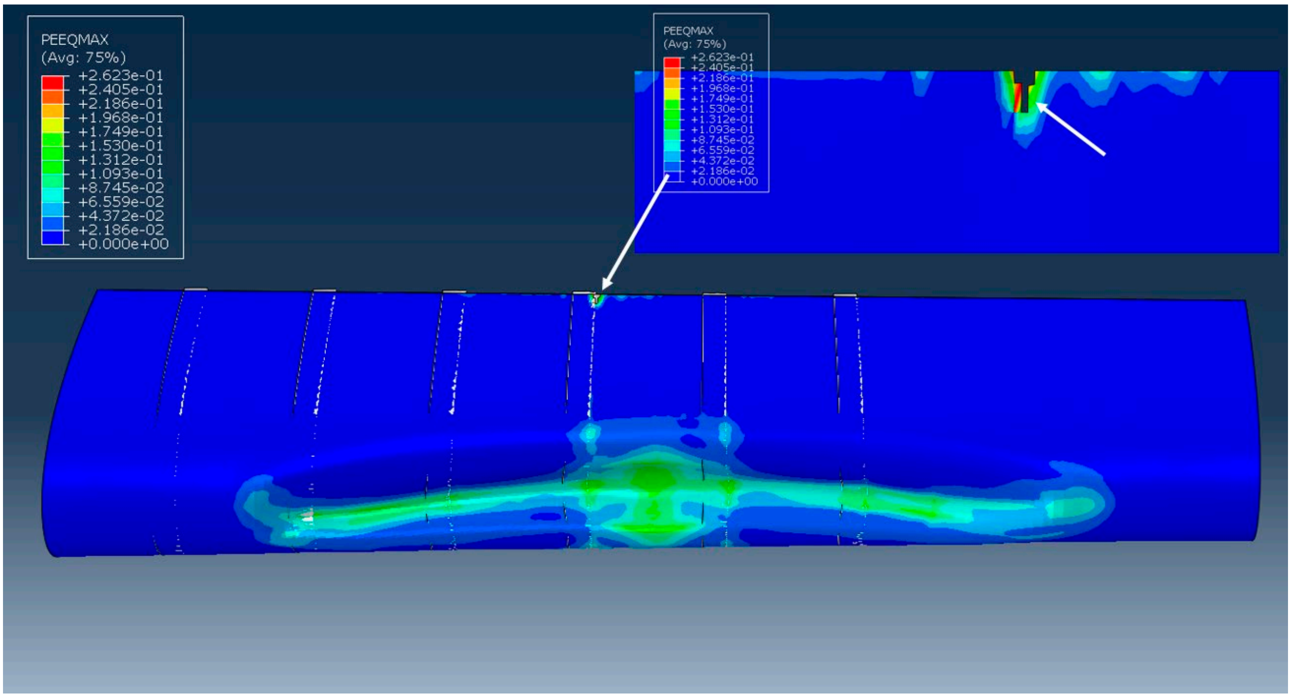

Figure 17: Skin rupture for a skin thickness of 2.0 [mm] after impact of the bird impactor at the location marked with the arrow. PEEQmax (plastic) strain [-] in the skin are above the material failure limit and skin tearing has taken place

The skin of 2 [mm] thick shows skin tearing at the connection with one of the ribs. Therefore, the skin thickness is adjusted once more to 2.5 [mm]. For the present leading edge geometry, a skin thickness of 2.5 [mm] is sufficient to withstand the bird impact under the simulated conditions in this work. This is shown in Figure 18 where the PEEQmax strain (plastic strain) of the impact are show. Thus, no skin tearing or penetration of the skin has taken place for a skin thickness of 2.5 [mm]. This skin thickness is used for the leading edge for the remainder of the simulations.

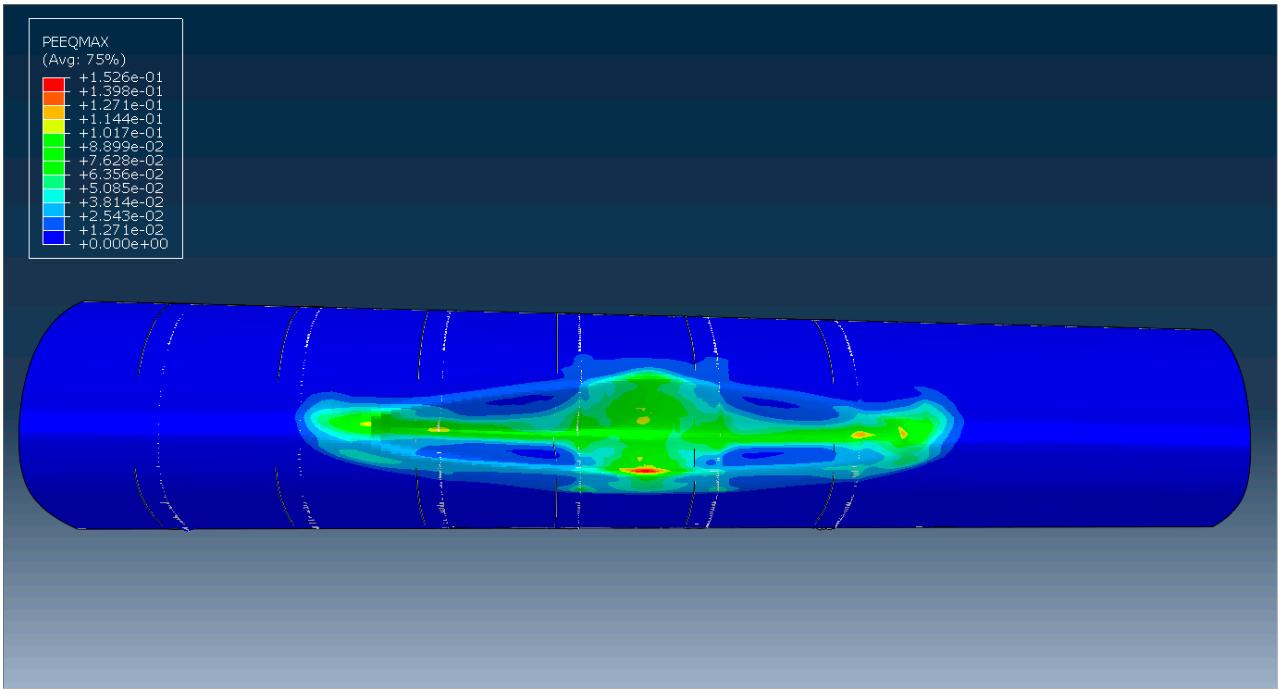

Figure 18: Skin impact result for impact with skin thickness 2.5 [mm]. PEEQmax (plastic) strain [-] in the skin are below material failure limit

4 Results leading edge impact

The leading edge for which impact with a bird impactor was simulated in the previous section is now targeted with the UAS model. First a single UAS is impacted on the leading edge for three different weights. Next, a multiple UAS impact is simulated for three UASs impacting the leading edge. Finally, a summary of the findings is presented.

4.1 Ballistic impact single UAS

The UAS's position with respect to the leading edge is determined via the battery pack which is the same as that of the bird impactor simulation, see Figure 19.

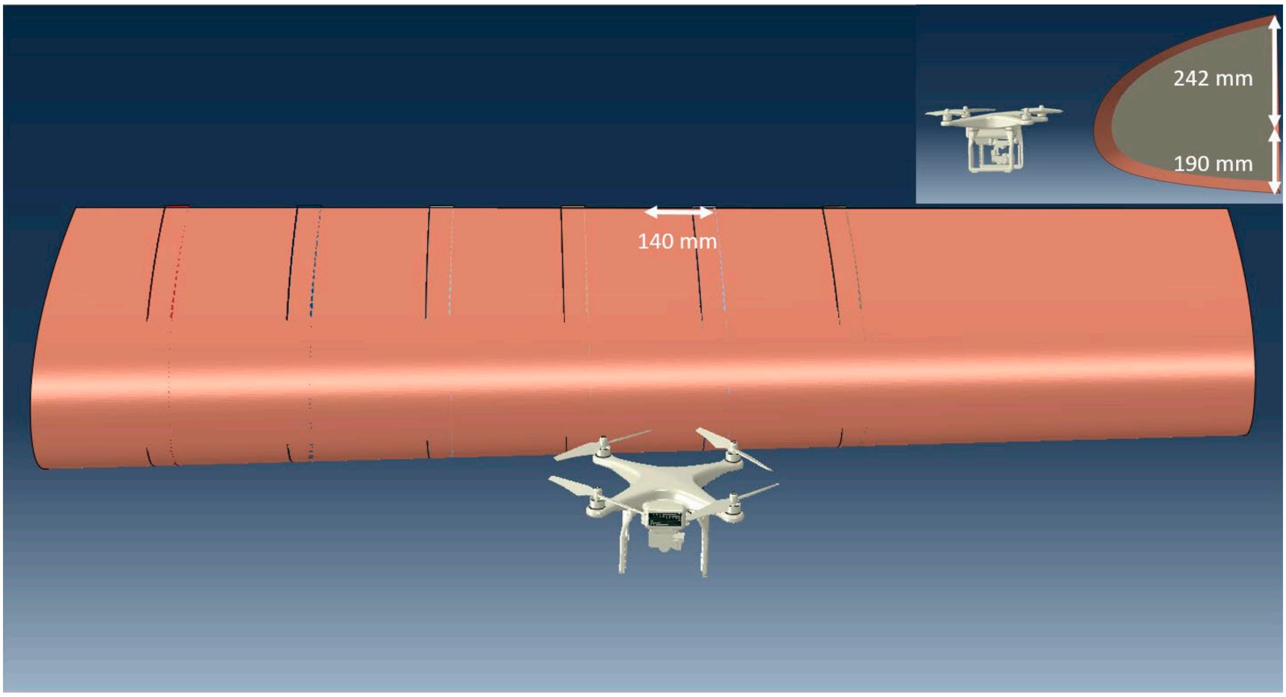

Figure 19: Positioning of the UAS with respect to the leading edge. The battery inside the UAS is located at the same position as the bird impactor

4.1.1 UAS 1.2 [kg]

Furthermore, the total mass of the UAS is 1216 [g] and the components weight are taken analogous to previous studies (13). Hence, the mass is computed as 4 times 50.7 [g] for motors, camera of 52.6 [g] and battery of 343 [g]. The remainder for the other components is: 617.6 [g]. This weight is assigned to UAS body, gimbal, and propellers. . The speed of the UAS is taken as 127 [m/s] (250 knots). This speed is motivated by the difference between UAS maximum speed and aircraft maximum speed. The type of UAS considered here reaches a maximum speed of 20 [m/s] and the aircraft speed (107 [m/s]) is taken as the maximum speed for a holding phase on a flight below 1829 [m] (6000 feet). A value for the aircraft that comes from paragraph 5-3-8-j.2 (a) of Aeronautical Information Manual (29). The same impact speed and motivation is recorded in other research as well (see e.g. (11), (13)).

The impact result is shown in Figure 20 where the UAS has impacted the leading edge. The close-up is showing that no components have entered the leading edge section. Skin tearing has taken place along the connection of skin and rib due to the large strains that are a result of the impact of the UAS as shown in Figure 21.

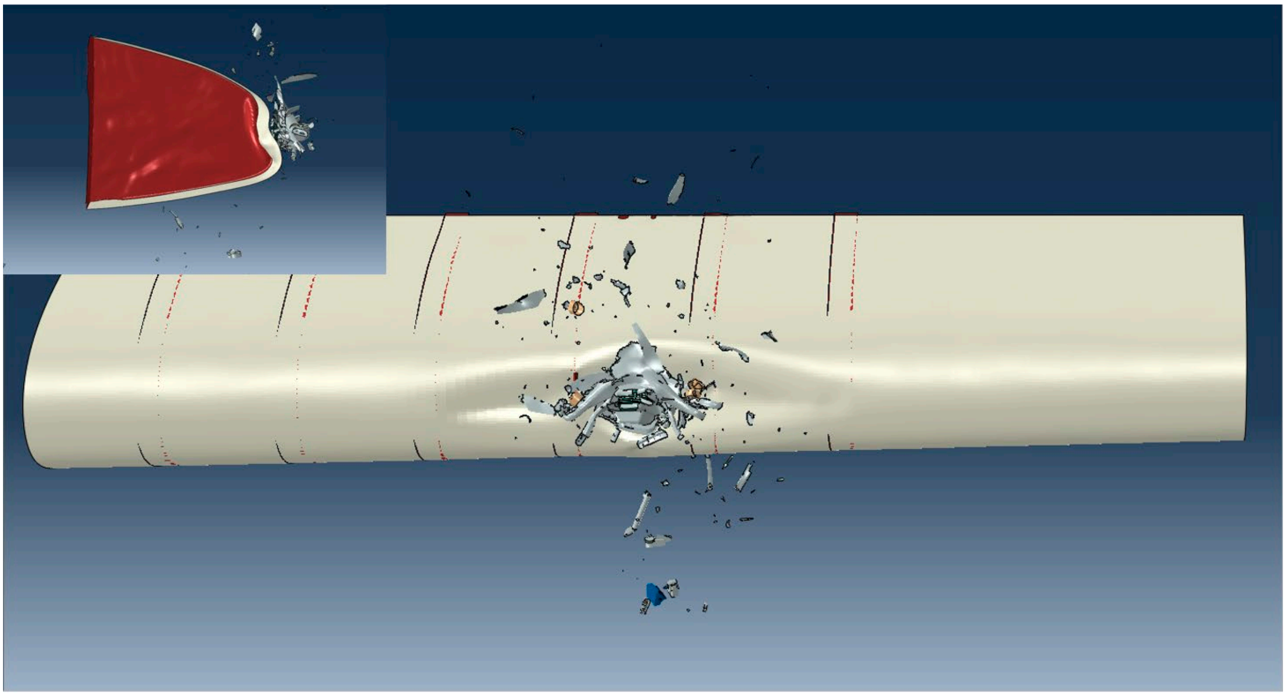

Figure 20: Deformation of the leading edge after UAS impact. Close-up and cut-out of the UAS impact zone showing no components are entering the leading edge

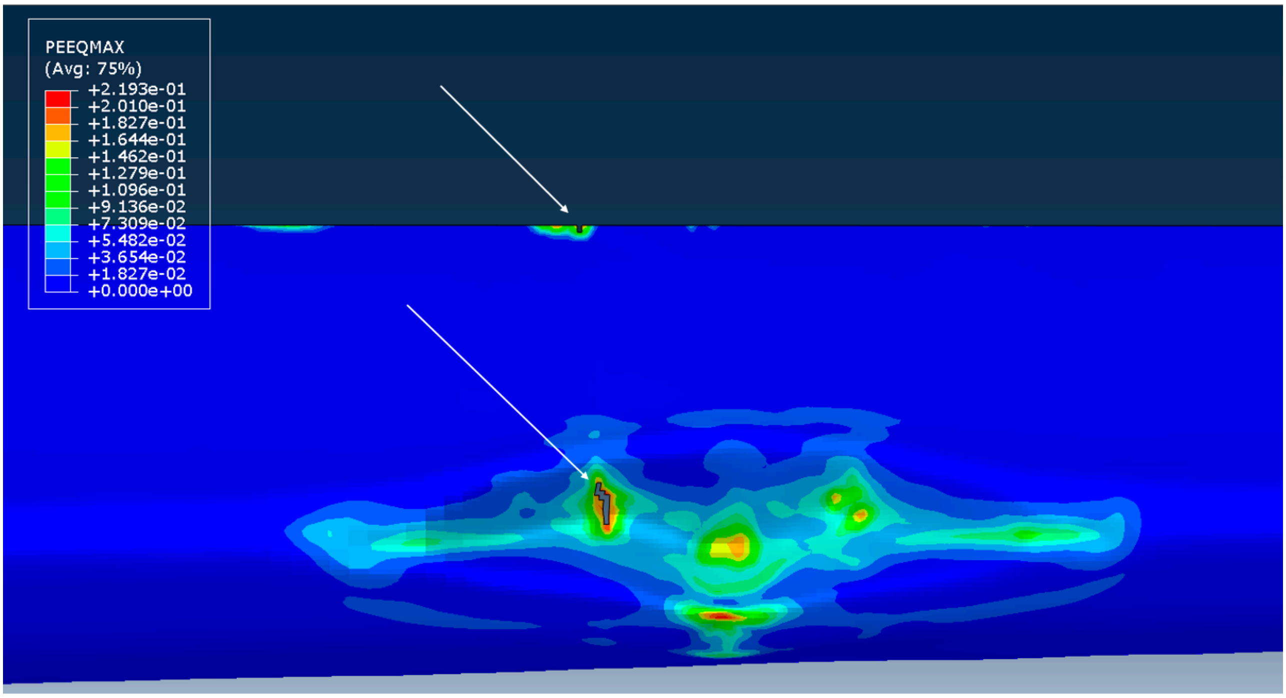

Figure 21: Contour plot of PEEQmax plastic strain [-]. The white indicators highlight the skin rupture where material failure has taken place. The image shows only the leading edge skin and the other components are suppressed

4.1.2 UAS 1.4 [kg]

The UAS model that the authors had access to was placed on a scale and the battery turned out to be slightly heavier than what was reported in literature. To see the effect of a heavier battery (438 [g] versus 343 [g]) the analysis was repeated with the heavier battery. In Figure 22 the damage caused by the impact is shown via a plot of PEEQmax strain and the skin tearing is clearly visible.

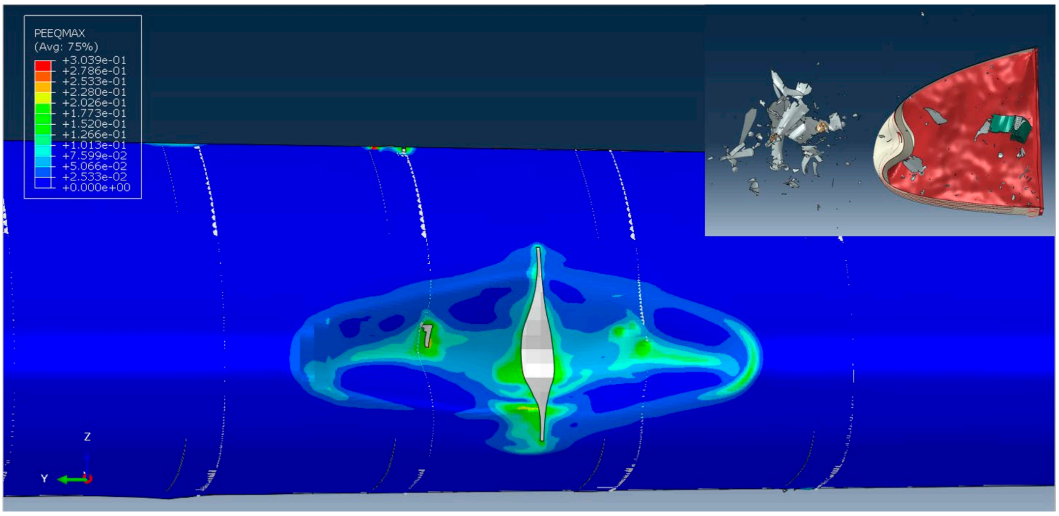

Figure 22: Contour plot of PEEQmax strain[-] and tearing of the skin after UAS impact with a heavier battery. Skin tearing has taken place on the location of impact and next to the rib. On the top side of the leading edge where the skin is connected to the spar, skin rupture has also occurred

Skin tearing has taken place and some of the UAS components have entered the leading edge. Most noticeably is the battery pack that has entered. Some of the battery cells are still largely intact. Hence, post impact short circuiting may pose a threat but this has not been investigated in this work. To show the deformation caused by the impact of the components (that entered the leading edge) onto the front spar the deformation is plotted in Figure 23.

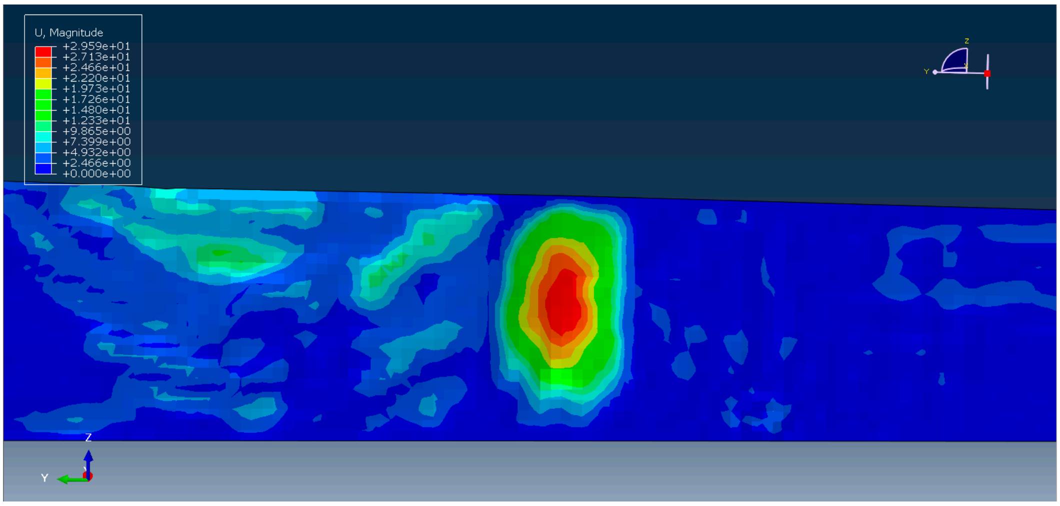

Figure 23: Maximum displacement of the spar due to the impact of the battery

Figure 23 shows that the maximum displacement during the impact is approximately 30 [mm]. Furthermore, no plastic deformation was computed. For this simulated impact no damage for the front spar was computed.

4.1.3 UAS 1.8 [kg]

To compare the impact of the UAS with the bird impactor the weight of the UAS is increased by multiplying all densities of the materials of the UAS by the same factor to arrive at a total weight of 1.81 [kg]. This is equivalent to the approaches documented in other literature (13) (14). The flight path is kept the same to all previous impact simulations with bird, 1.2 [kg] UAS and UAS with heavier battery. The PEEQmax strain of the impact of the 1.81 [kg] UAS are plotted in Figure 24 on the deformed leading edge. Tearing of the skin is visible and part of the UAS has entered the wing leading edge. The components that enter the leading edge are made visible with a cut-out of the impact as shown in Figure 25.

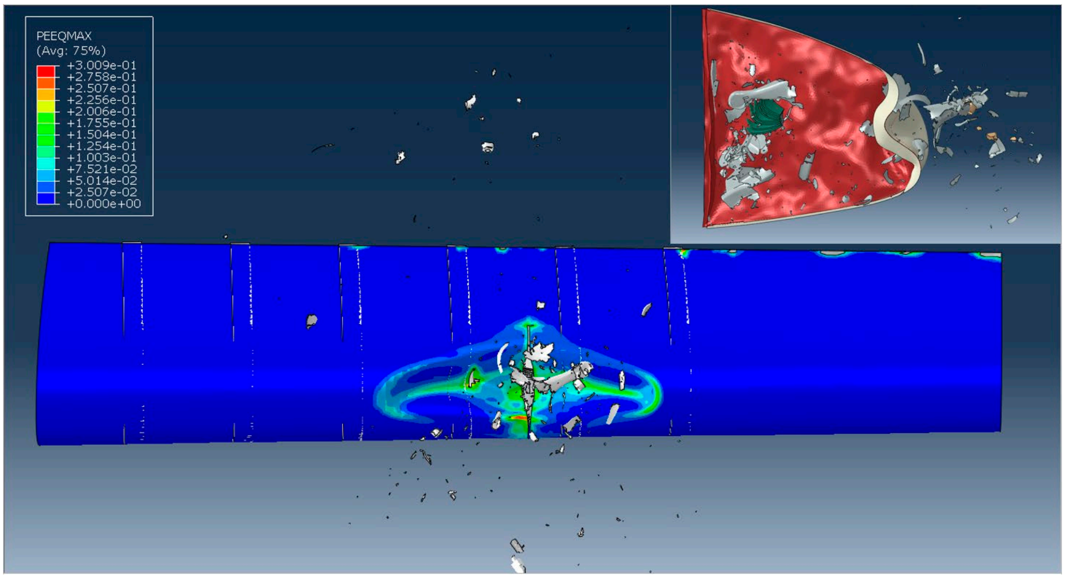

Figure 24: Contour plot of PEEQmax strain [-] of the UAS impacting the wing leading edge. A large tearing of the skin is visible at the location of impact

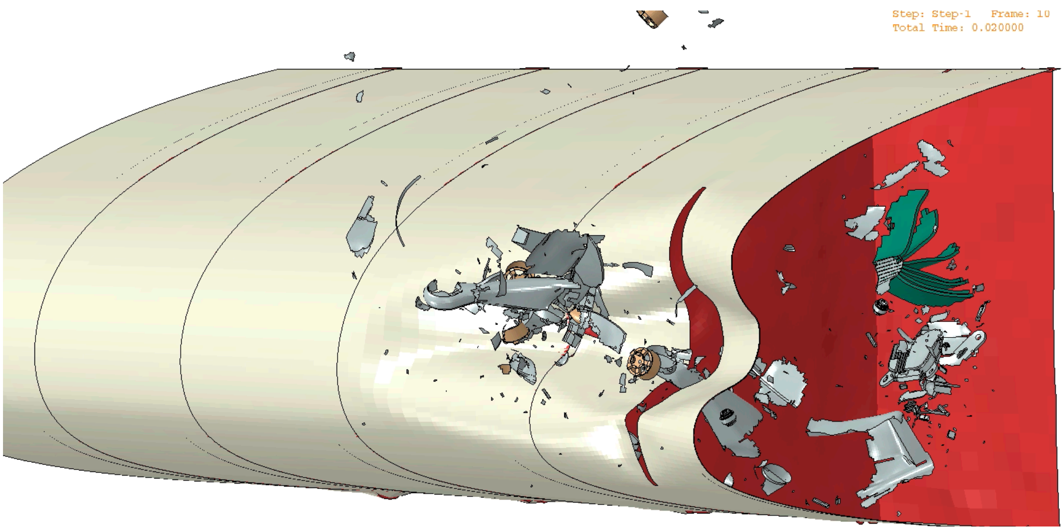

Figure 25: UAS components entering the wing leading edge. The battery pack (green) has entered the wing but is completely destroyed. The image shows a cut-out of the wing leading edge where the UAS enters the structure

The battery package (green) has entered the wing leading edge. In the current model the package of loose cells are partly intact. Therefore, it is of interest to further detail the battery model to include electric-thermal properties and determine if this poses additional risk on the structure. Furthermore, the results show that the current FEA approach is a good means to track components of the UAS. For example, the brown coloured motors are still identifiable. The components that have entered the leading edge and have impacted the front spar did not damage the front spar. The maximum displacements calculated for the front spar are shown in Figure 26. Maximum displacement is 59 [mm] and no plastic deformation was computed. For this simulated impact the front spar was not damaged. Hence, the impact of a single UAS does not damage the front spar for the cases considered in this work.

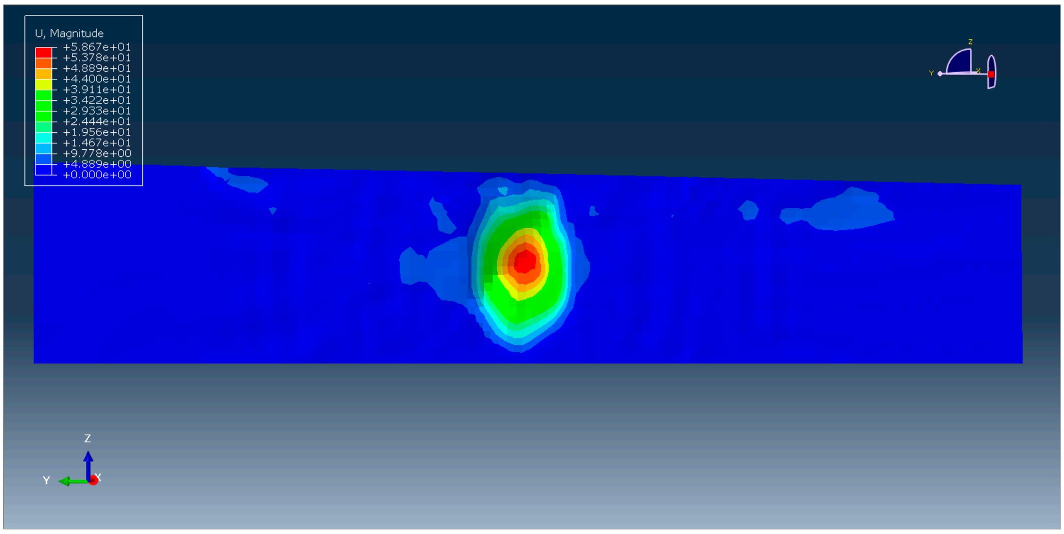

Figure 26: Maximum displacement [mm] contour plot of the front spar after impact with the components of the 1.8 [kg] UAS

4.2 Results – ballistic impact multiple UAS

The effect of a multiple UAS impact is modelled using the previously introduced leading edge and copying the UAS model.

4.2.1 UASs 1.2 [kg]

In the present study, three UASs of 1.2 [kg] each are impacted on the leading edge one at a time. Although many combinations of impact scenario are possible a scenario is selected where all three UASs hit the leading edge in-between the same ribs. Furthermore, the distance between the UASs is chosen such that the skin has largely absorbed the impact from one UAS before the second UAS hits the skin. In this case the distance between UAS 1 and UAS 2 is 2.5 [m] and the distance between UAS 2 and UAS 3 is 4.5 [m]. In addition, the UASs hit the leading edge such that they do not bounce off entirely or in part. At least the battery of the UAS has to hit the leading edge or spar. Finally, the second and third UAS are hitting debris of the first and second UAS while impacting the leading edge. The effect of the UAS hitting debris on the impact is not further investigated. In Figure 27 the three UASs are shown together with the leading edge at several time steps through the simulation from both the top view (left) and the bottom view (right). A closer look at the location of impact of the UASs is shown in Figure 28.

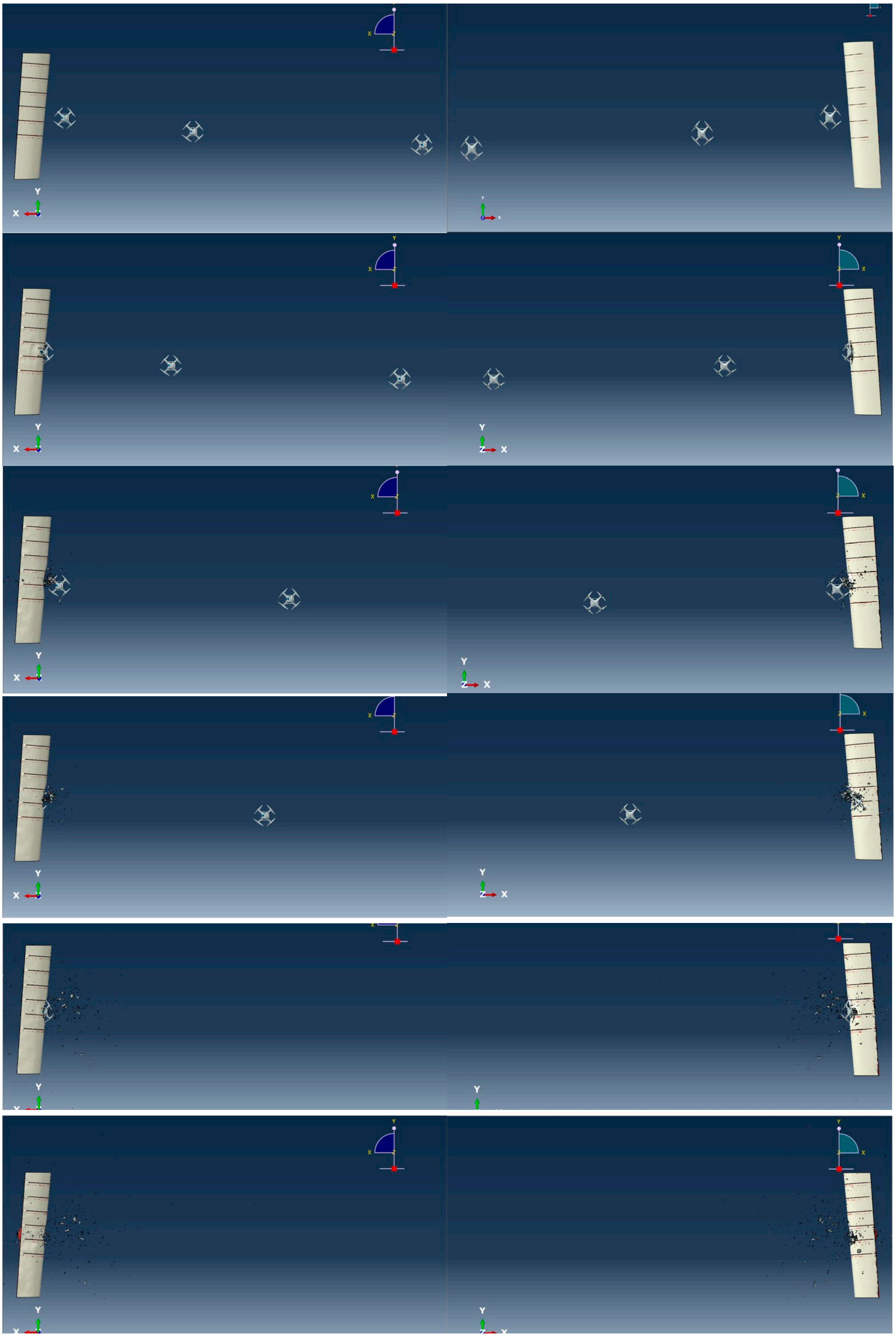

Figure 27: Multiple UAS impact simulation setup. Three UASs are aligned with respect to the leading edge to impact in-between the same ribs. Zone of impact is between the same ribs as in the previous single UAS impact

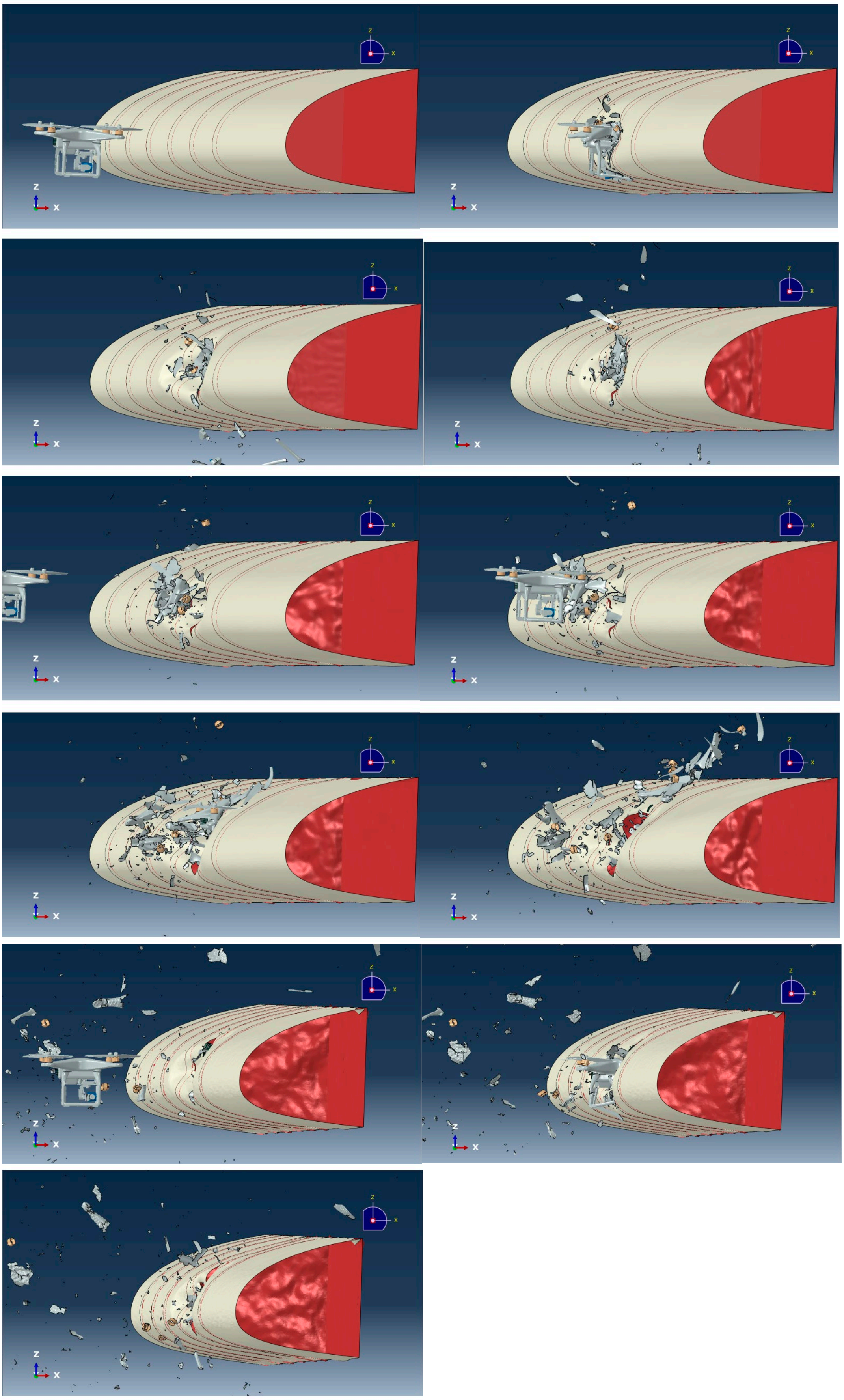

Figure 28: Sequence of events of the three UASs impacting the leading edge

As can be seen from Figure 28 the first UAS impacts the wing in the same way the single UAS impact was modelled. The second UAS impacts near the same location but some debris moves over the leading edge skin. The third UAS impacts the wing and is completely destroyed. From the front of the leading edge the impact of the three UASs is show in Figure 29.

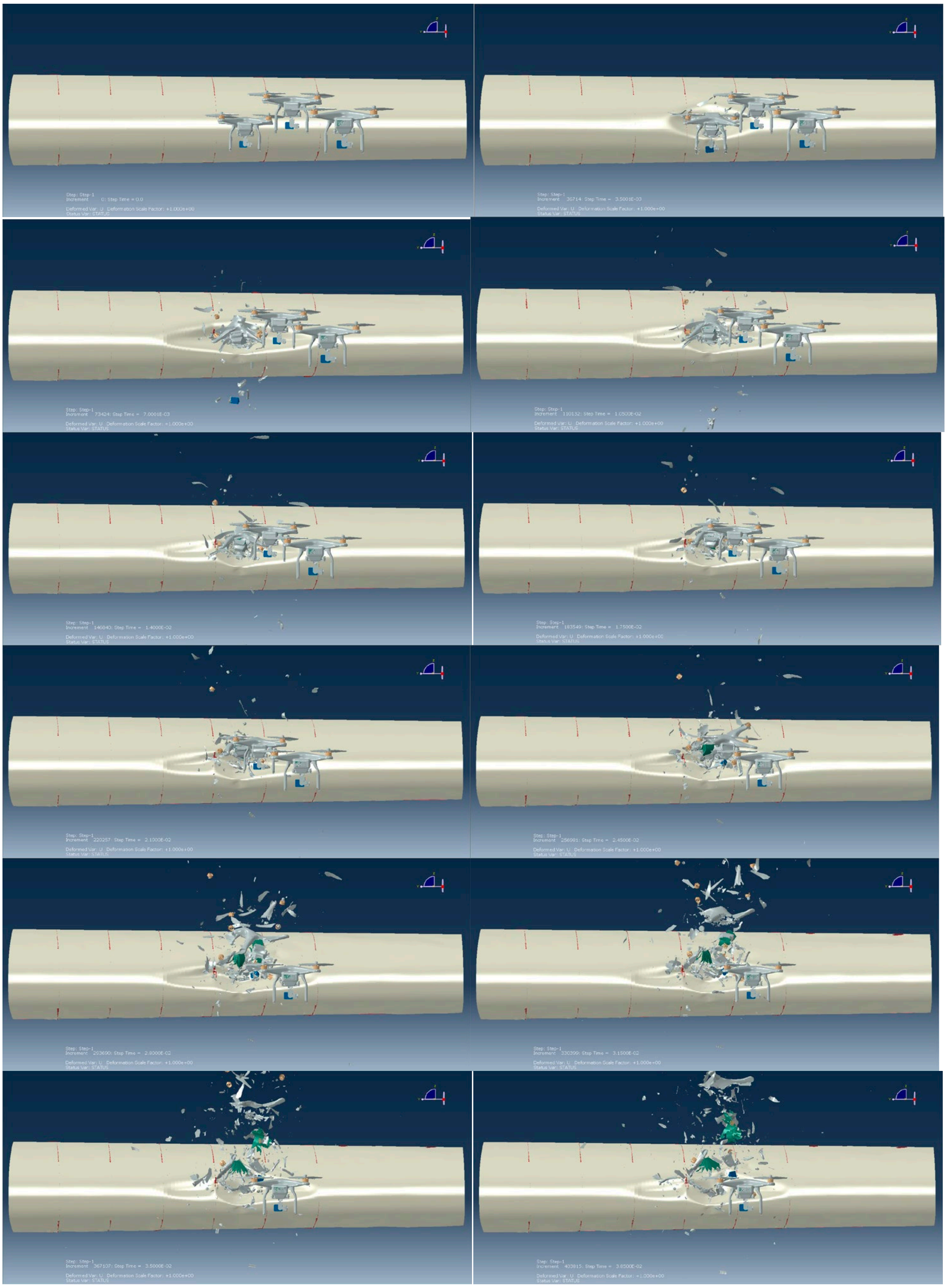

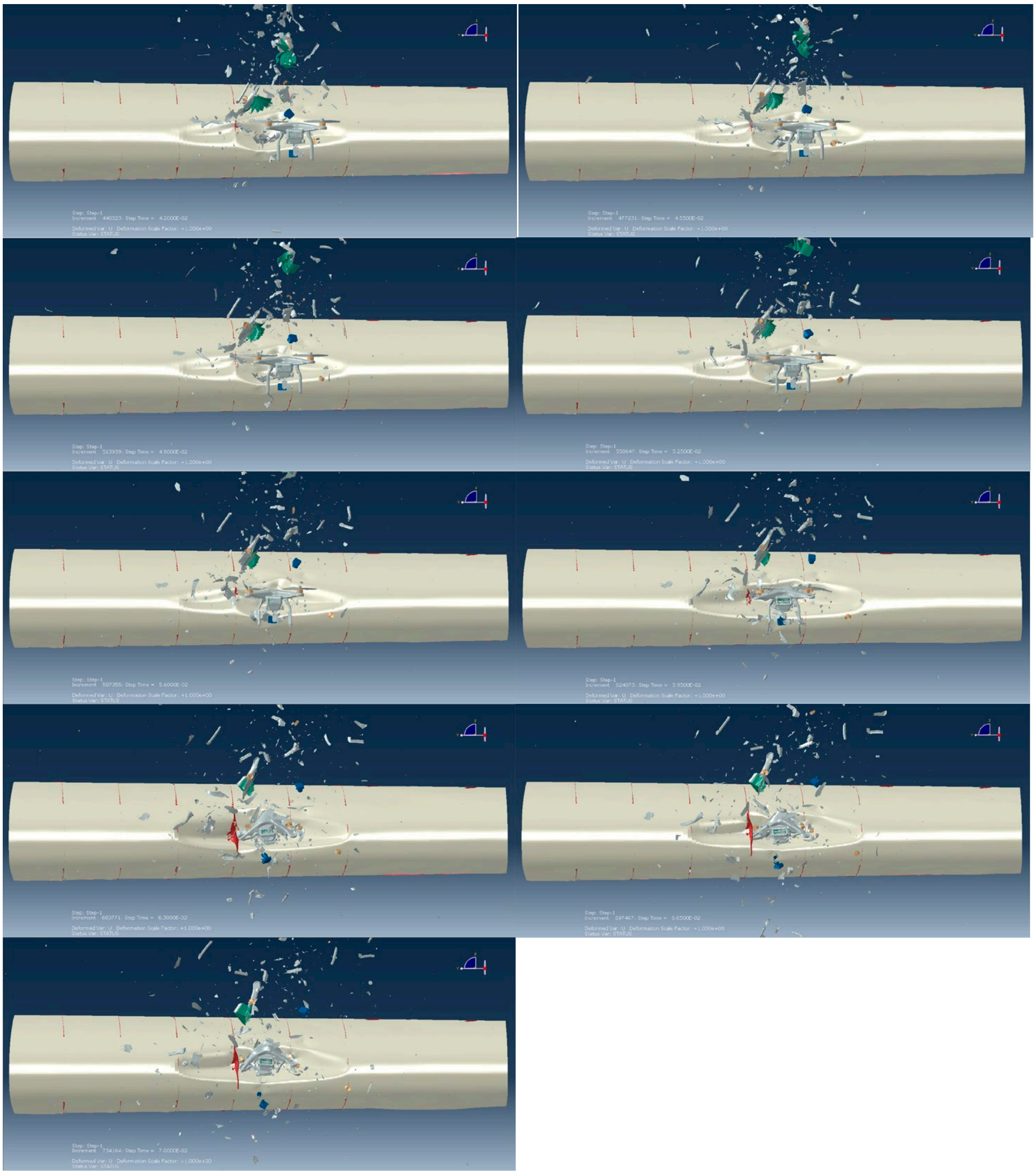

Figure 29: Sequence of events of the three UASs impacting the leading edge. Frontal view of the leading edge

Figure 30 shows the impact locations from the frontal view of the leading edge. The impact of the first UAS is the same as that of the single UAS impact. Second impact caused by the next impacting UAS is slightly less severe as part of the first UAS is colliding with the second UAS. The third impact is causes the leading edge skin to detach from one of the ribs. Once all UASs have impacted the leading edge a deformation plot of the damage can be created. In Figure 30 the PEEQmax strains are plotted on the deformed structure. Compared to the single UAS impact, the skin tearing is larger in the skin at the location where it is connected to the rib. In addition, two of the components of the third UAS enter the wing skin. The components that enter the wing are shown in a cut-out of the leading edge in Figure 31.

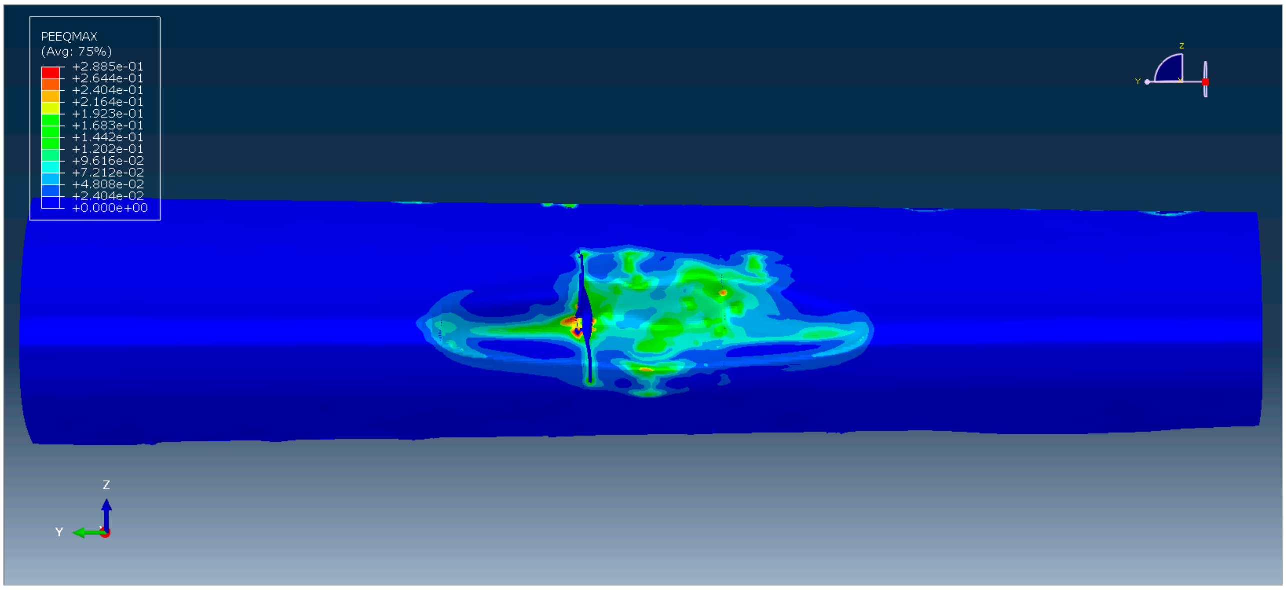

Figure 30: Skin tearing of the wing leading edge. Colours are PEEQmax(plastic) strains plotted on the geometry

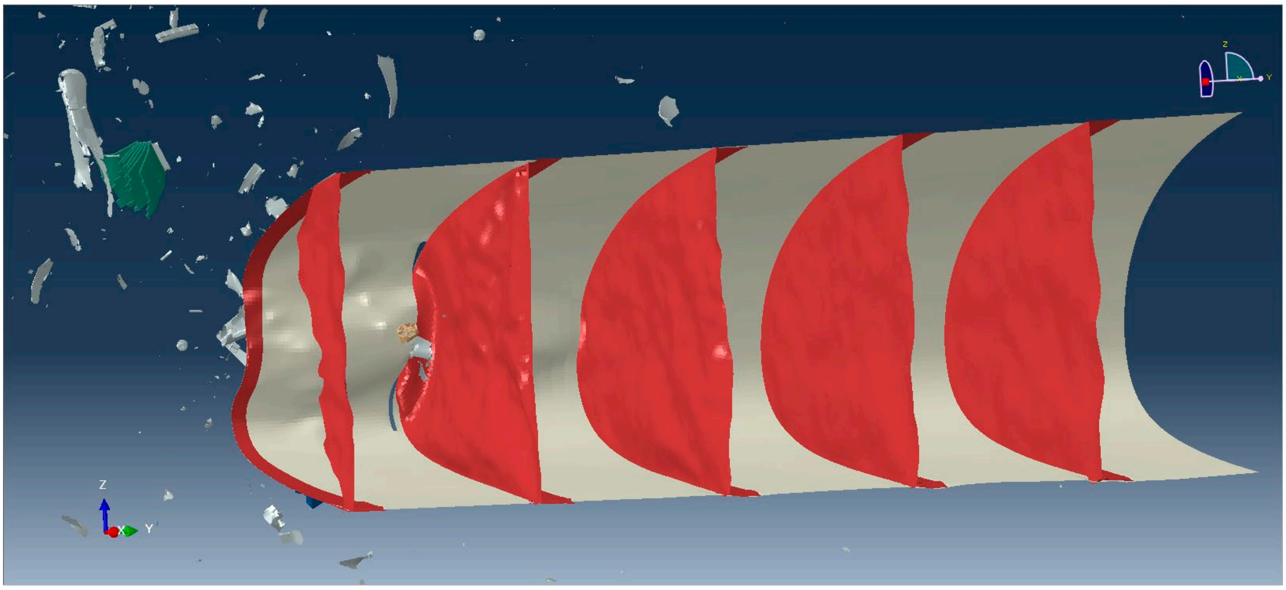

Figure 31: Multiple UAS impact, one engine component (brown) and part of the UAS housing grey of the third UAS have entered into the wing leading edge. Parts of the model view have been cut away to show the leading edge internals

Figure 31 shows that most debris remains outside the wing leading edge. However, one engine from the third UAS and part of the UAS housing have entered the leading edge. The maximum deformation that the impact of these components cause on the front spar is shown in Figure 32. In Figure 32 no damage has been computed on the front spar. The maximum deformation in between the two ribs where the impacts have taken place is 13 [mm] deflection of the front spar.

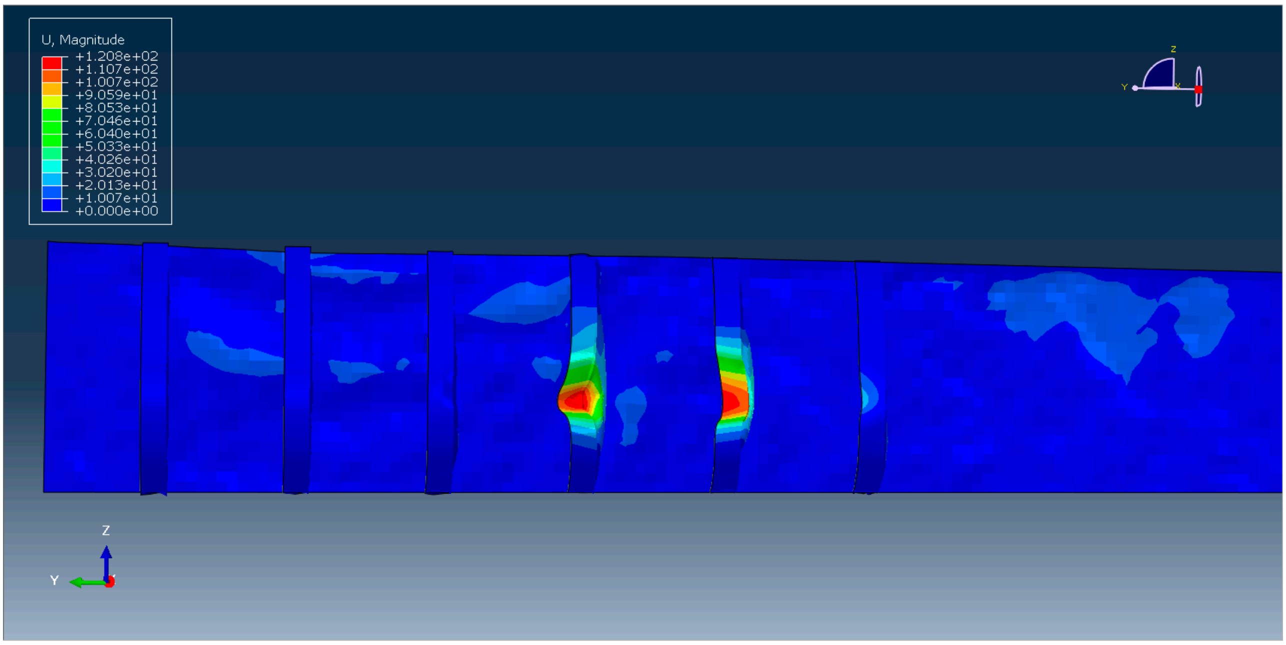

Figure 32: Maximum deformation [mm] contour plot on the deformed spar and ribs after the third UAS impact. The maximum deflection occurs on the ribs and deflection of the spar is negligible

4.2.2 UASs 1.8 [kg]

For completeness, the heavier UAS of 1.81 [kg] is impacted onto the leading edge as well with three UASs. The resulting impact damage is shown in Figure 33. The damage on the leading edge is larger than for the single UAS. The front spar shows a larger deformation than with the 1.2 [kg] drones as shown in Figure 34. Although the deformation is much larger no material failure is computed and the front spar has not been penetrated with UAS components.

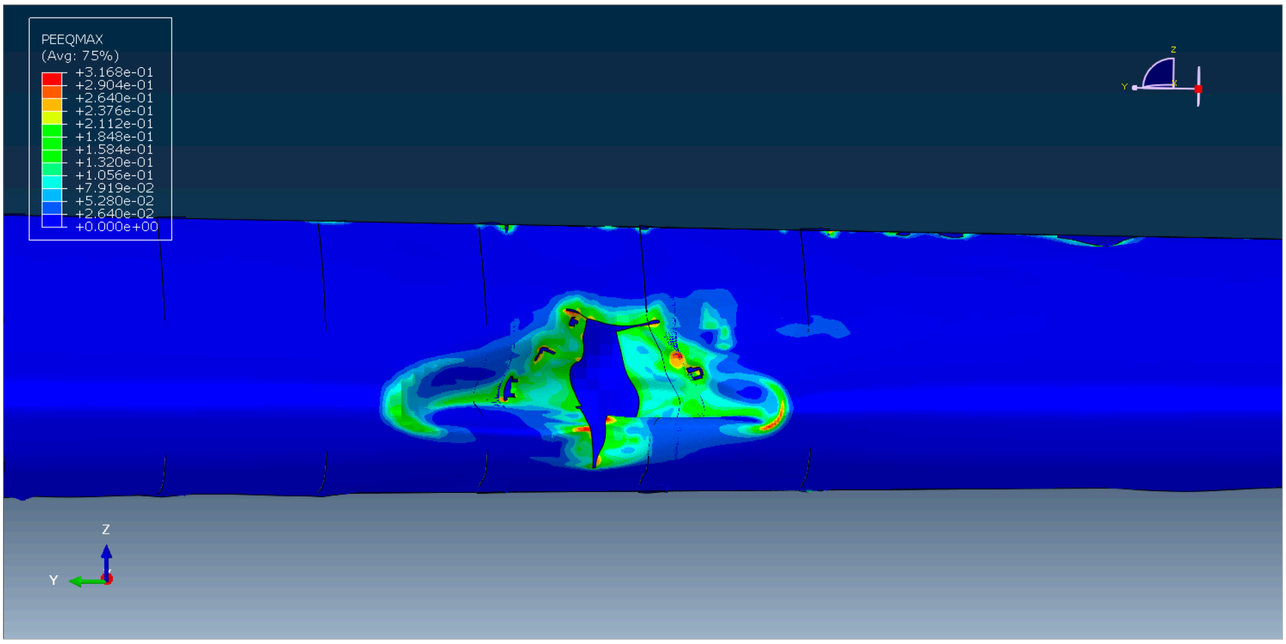

Figure 33: PEEQMax plastic strain [-] contour plot. Skin tearing observed after a multiple 1.81 [kg] UAS impact

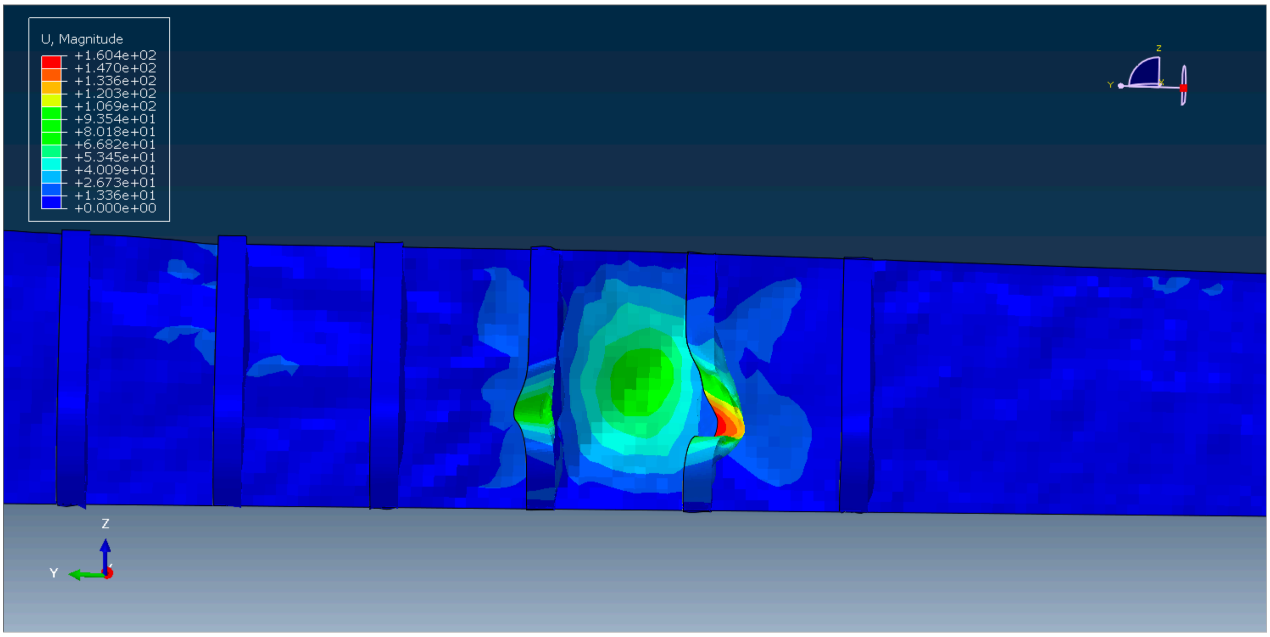

Figure 34: Maximum deformation [mm] contour plot on the deformed spar and ribs after the third UAS impact

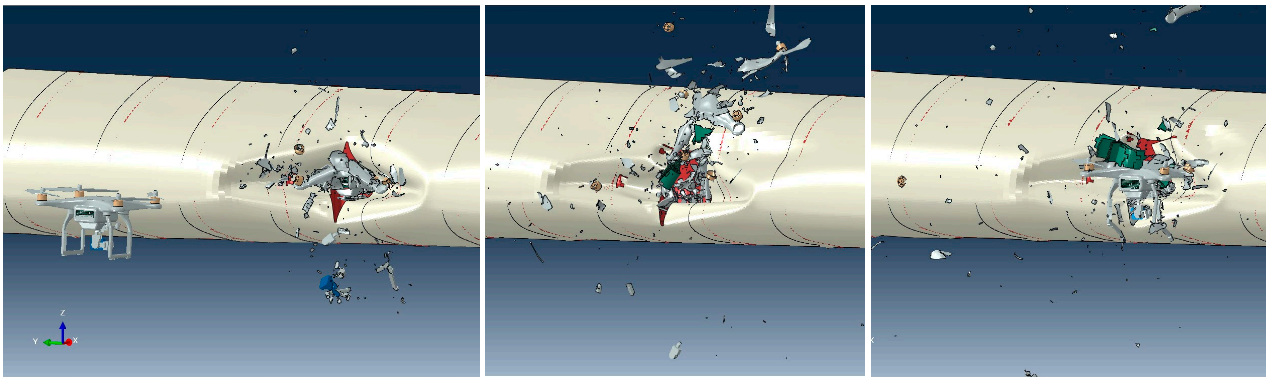

Figure 35: Impact of each individual UAS. From left to right, the first UAS enters the leading edge. The second UAS breaks up and partly enters the wing. The third UAS enters the wing but collides with the debris of the previous UAS components

The maximum deformation that is computed between the two ribs due to the impact of the third UAS is 90 [mm]. The sequence of impacts is shown in Figure 35. In Figure 35 the first UAS impacts the skin and tears the skin open. The second UAS breaks up and part of the components enter the leading edge and other parts bounce off. The third UAS flies into the opening created by the previous impacts. However, the third UAS breaks up as well due to the opening being smaller than the size of the UAS. Most part of each UAS has entered the leading edge as can be seen in Figure 36.

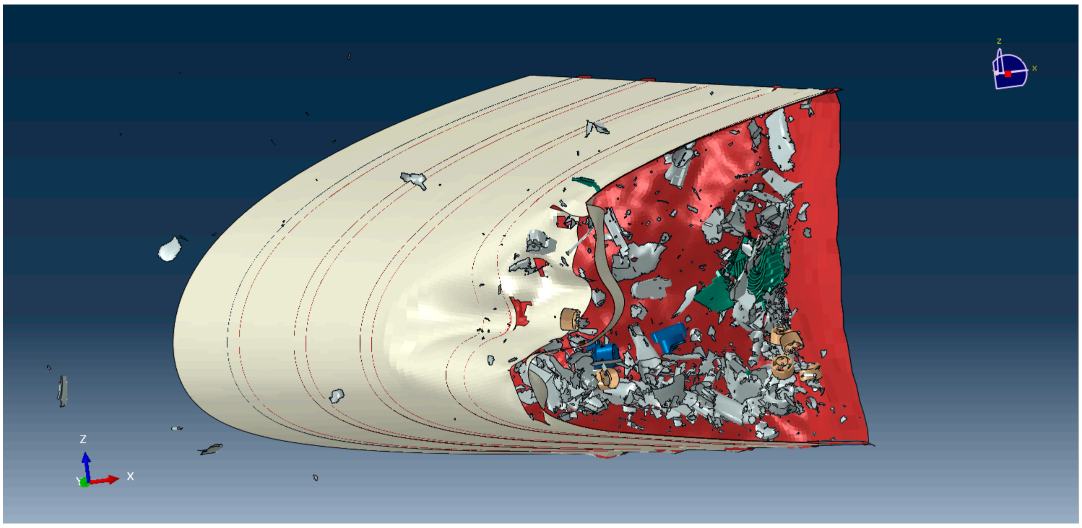

Figure 36: UAS components of the three 1.81 [kg] UASs have entered the leading edge section. None of the battery packs (green) appears to be intact after the impact but individual cells are still visible

The cut-out of the leading edge shows the components of the UASs ending up into the wing leading edge after the impact. None of the components appears to be intact. Hence, the battery pack used in the present modelling where the battery consists of individual cells is destroyed after impact but individual cells may still pose a threat. A different modelling of the battery such as was done in (13) or (14) where the battery is modelled as a single component may give different results but a post-impact analysis via e.g. electro-thermal analysis of the battery cells is part of ongoing research.

4.3 Summary

To summarize the impact studies carried out in this work Table 11 gives an overview of the impact condition and the damage observed. To summarize, heavier UAS components penetrate the leading edge considered in this work and may cause deformation of the spar. When multiple UAS impact on the area between the ribs for the leading edge considered here the damage of leading edge skin is larger and the deformation of the spar is larger.

Table 11: Summary of impact studies performed and the damage observed

	Leading edge skin	**UAS components inside leading edge**	**Front spar deformed**
Single UAS 1.2 [kg]	Skin tearing, no penetration	None	No
Single UAS 1.4 [kg] (heavier battery)	Skin rupture, penetration of components	Yes, battery and housing	Yes, max 30 [mm]
Single UAS 1.8 [kg]	Skin rupture, UAS mostly inside leading edge	Yes, almost all components	Yes, max 59 [mm]
Multiple UAS 1.2 [kg] per UAS	Skin rupture, some components penetrate skin	Yes, engine and part of drone housing	Yes, max 13 [mm]
Multiple UAS 1.8 [kg] per UAS	Skin rupture, UASs end up inside the leading edge	Yes, almost all components of all three UASs.	Yes, max 90 [mm]

5 Conclusions and Recommendations

In this work a UAS model was developed analogous to previous research found in the open literature. The modelling efforts adopted to model the individual components gave similar ballistic impact results as those that could be expected based on literature recordings.

A preliminary wing leading edge design was created that sustains a simulated bird impact for the conditions considered in this work. This impact was simulated via an impactor that was created analogous to previous literature reporting. A UAS impact on this leading edge for a reasonably sized UAS showed that skin tearing takes place which raises concerns over what would happen to equipment that is located right behind the wing leading edge. Furthermore, an impact with a UAS fitted with a heavier battery resulted in the battery entering the leading edge. The battery was destroyed but battery cells were partly intact under the modelled conditions in this work. A post impact analysis of these cells to determine short-circuiting risks was out of scope for the present work.

To show the difference between a bird impact and a UAS impact with the same weight a heavier UAS was modelled as well. Here significant damage is visible on the leading edge skin. Furthermore UAS components enter the wing including the battery pack. In the present study the battery pack was destroyed upon impact but individual cells appeared to be intact under the modelled conditions. For all three simulated cases the front spar deformed but there was no material failure due to the components that did manage to enter the leading edge.

The multiple UAS impact showed an increase in damage sustained by the leading edge. For the 1.2 [kg] UAS two components entered the wing leading edge but for the UAS of 1.81 [kg] all three UASs ended up partly or completely inside the leading edge. All three UASs and their components were not intact after impact. For all simulated cases the front spar deformed to a larger extend than with the single UAS impact. However, no material failure was observed in the spar.

For future work, it is recommended to investigate the response of composite wing leading edges. This material behaves different on impact as opposed to metal and components of the UASs may behave differently on post impact. Furthermore, it is recommended to investigate the modelling of the battery pack itself. Different modelling approaches may show different results both on impact on the leading edge as well as post-impact behaviour. For example, a softer battery may stay intact and may necessitate an electro-thermal-mechanical analysis to see if the battery short circuits.

The UAS impact models developed for this study can be used by authorities and the industry to analyze different threat scenarios involving medium sized UASs. With the developed models further insight in the damage behavior is obtained and expensive impact tests can be reduced. Moreover, studies like these can be input for possible design changes for aircraft.

6 Bibliography

1. **EASA.** Certification Specifications CS-25 Large Aeroplanes. [Online] 2020. [Cited: 15 01 2021.] https://www.easa.europa.eu/certification-specifications/cs-25-large-aeroplanes.
2. **FAA.** Electronic Code of Federal Regulations - PART 25 AIRWORTHINESS STANDARDS: TRANSPORT CATEGORY AIRPLANES. [Online] 2021. [Cited: 15 01 2021.] https://www.ecfr.gov/cgi-bin/text-idx?SID=1fab3f89ba09fe822716daf4d917ec8a&mc=true&tpl=/ecfrbrowse/Title14/14cfr25_main_02.tpl.
3. **Dennis, N. and Lyle, D.** *Bird strike damage & windshield bird strike.* ATKINS. s.l. : European Aviation Safety Agency, 2009.
4. **EASA.** *Annual Safety Review 2019.* s.l. : European Union Aviation Safety Agency, 2019.
5. **Sharma, R.S.** *Investigation into Unmanned Aircraft System Incidents in the National Airspace System.* 2016.
6. **Radi, A.** *Potential Damage Assesment of a mid-air collision with a small uav.* s.l. : CASA, 2013.
7. **British Military Aviation Authority.** *Small remotely piloted aircraft systems drone midair collision study.* London : Crown, 2016.
8. **EASA.** *'Drone Collision' Task Force.* s.l. : European Aviation Safety Agency, 2016.
9. **ASSURE.** ASSURE UAS Airborne Collision Severity Evaluation Final Report. [Online] 2017. [Cited: 13 11 2020.] https://www.assureuas.org/projects/deliverables/sUASAirborneCollisionReport.php.
10. **Olivares, G., et al.** *UAS Airborne Collision Severity Evaluation Executive Summary - Structural Evaluation.* Washington : U.S. Department of Transportation Federal Aviation Administration DOT/FAA/AR-xx/xx, 2017a.
11. **Olivares, G., et al.** *UAS Airborne Collision Severity Evaluation - Volume II - Quadcopter.* s.l. : Federal Aviation Administration, 2017b.
12. **Olivares, G., et al.** *UAS airborne collision severity evaluation - volume III - fixed wing.* s.l. : Federal Aviation Administration, 2017c. Report DOT/FAA/AR-XX/XX.
13. **Drumond, T., Greco, M. and Cimini, C.** *Evaluation of Increase Weight in a Wing Fixed Leading Edge Design to Support UAS Impact.* Sweden : s.n., 2019.
14. **Jonkheijm, L.** *Predicting helicopter damage caused by a collision with an Unmanned Aerial System using explicit Finite Element Analysis.* Delft : TU Delft, 2020.
15. **Austen, W. J., Lord, Steven J. and Bridges, Simon A.** *Vulnerability of manned aircraft to drone strikes.* s.l. : EASA.2020.C04 Qinetiq, 2020.
16. **BBC.** Gatwick Airport: Drones ground flights. *BBC News.* [Online] 20 12 2018. https://www.bbc.com/news/uk-england-sussex-46623754.
17. **Calder, Simon.** GATWICK DRONE DISRUPTION COST OVER £50M. [Online] 2019. [Cited: 22 01 2021.] https://www.independent.co.uk/travel/news-and-advice/gatwick-drone-airport-cost-easyjet-runway-security-passenger-cancellation-a8739841.html.
18. **Wendt, P., Voltes-Dorta, A. and Suau-Sanchez, P.** *Estimating the costs for the airport operator and airlines of a drone-related shutdown: an application to Frankfurt international airport.* 2020. pp. 1-24.
19. **EASA.** *ASIDIC EASA UAS Collision Workshop.* 2017.

20. **Kota, K. R., et al.** *Development and validation of finite element impact models of high-density UAS components for use in air-to-air collision simulations.* 2020. pp. 1178-1199.

21. **Yu, J., et al.** *Numerical simulation of a UAV impacting engine fan blades.* 2021.

22. **Simulia.** *Abaqus - Abaqus analysis user's guide.* s.l. : Dassault Systemes, 2020. Version 2020.

23. **Rice, Richard C., et al.** *Metallic Materials Properties Development and Standardization (MMPDS).* Washington : U.S. Department of Transportation Federal Aviation Administration, 2003.

24. **KAY, G.** *Failure Modeling of Titanium 6Al-4V and Aluminium 2024-T3 With the Johnson-Cook Material Model.* s.l. : Report DOT/FAA/AR-03/57, FAA, 2003.

25. **McNaughtan, I.** *The design of leading-edge and intake wall structure to resist bird impact.* s.l. : Royal Aircraft Establishment, 1972.

26. **Riccio, A., Cristiano, R. and Saputo, S.** *A brief introduction to the bird strike numerical simulation.* 2016.

27. **Segletes, S. B.** *An analysis on the stability of the Mie-Gruneisen equation of state for describing the behavior of shock loaded materials.* Aberdeen Proving Ground, Maryland : Ballistic Research Laboratory, 1991. Technical Report BRL-TR-3214.

28. **Walvekar, V., et al.** *BIRDSTRIKE ANALYSIS ON LEADING EDGE OF AN AIRCRAFT WING USING A SMOOTH PARTICLE HYDRODYNAMICS BIRD MODEL.* Vancouver : Proceedings of the ASME 2010 International Mechanical Engineering Congress & Exposition, 2010.

29. **Federal Aviation Administration.** *Aeronautical Information Manual. Official Guideline to Basic Flight Information and ATC Procedures.* 2017.

Dedicated to innovation in aerospace

Royal NLR - Netherlands Aerospace Centre

NLR operates as an objective and independent research centre, working with its partners towards a better world tomorrow. As part of that, NLR offers innovative solutions and technical expertise, creating a strong competitive position for the commercial sector.

NLR has been a centre of expertise for over a century now, with a deep-seated desire to keep innovating. It is an organisation that works to achieve sustainable, safe, efficient and effective aerospace operations.
The combination of in-depth insights into customers' needs, multidisciplinary expertise and state-of-the-art research facilities makes rapid innovation possible. Both domestically and abroad, NLR plays a pivotal role between science, the commercial sector and governmental authorities, bridging the gap between fundamental research and practical applications. Additionally, NLR is one of the large technological institutes (GTIs) that have been collaborating over a decade in the Netherlands on applied research united in the TO2 federation.

From its main offices in Amsterdam and Marknesse plus two satellite offices, NLR helps to create a safe and sustainable society. It works with partners on numerous programmes in both civil aviation and defence, including work on complex composite structures for commercial aircraft and on goal-oriented use of the F-35 fighter. Additionally, NLR helps to achieve both Dutch and European goals and climate objectives in line with the Luchtvaartnota (Aviation Policy Document), the European Green Deal and Flightpath 2050, and by participating in programs such as Clean Sky and SESAR.

For more information visit: **www.nlr.org**

Postal address
PO Box 90502
1006 BM Amsterdam, The Netherlands
e) info@nlr.nl i) www.nlr.org

Royal NLR
Anthony Fokkerweg 2
1059 CM Amsterdam, The Netherlands
p) +31 88 511 3113

Voorsterweg 31
8316 PR Marknesse, The Netherlands
p) +31 88 511 4444